

JGR Solid Earth

RESEARCH ARTICLE

10.1029/2022JB024139

Key Points:

- We conducted a series of experiments of unconfined lava flow using bubbly syrup particle suspension
- The heterogeneous distribution of bubbles and particles changes the fluid rheology, affecting the flow velocity and morphology
- The vertical separation of bubbles, generating a liquid-rich bottom layer, concentrates the bubble to generate a cavernous shelly pahoehoe

Supporting Information:

Supporting Information may be found in the online version of this article.

Correspondence to:

A. Namiki,
namiki@eps.nagoya-u.ac.jp

Citation:

Namiki, A., Lev, E., Birnbaum, J., & Baur, J. (2022). An experimental model of unconfined bubbly lava flows: Importance of localized bubble distribution. *Journal of Geophysical Research: Solid Earth*, 127, e2022JB024139. <https://doi.org/10.1029/2022JB024139>

Received 31 JAN 2022

Accepted 18 MAY 2022

Author Contributions:

Conceptualization: Atsuko Namiki

Data curation: Jasper Baur

Formal analysis: Atsuko Namiki

Funding acquisition: Atsuko Namiki, Einat Lev

Investigation: Atsuko Namiki, Janine Birnbaum, Jasper Baur

Methodology: Atsuko Namiki, Einat Lev

Software: Atsuko Namiki, Einat Lev

Supervision: Einat Lev

Validation: Atsuko Namiki

Visualization: Atsuko Namiki

Writing – original draft: Atsuko Namiki

Writing – review & editing: Atsuko Namiki, Einat Lev, Janine Birnbaum

© 2022. The Authors.

This is an open access article under the terms of the [Creative Commons Attribution License](#), which permits use, distribution and reproduction in any medium, provided the original work is properly cited.

An Experimental Model of Unconfined Bubbly Lava Flows: Importance of Localized Bubble Distribution

Atsuko Namiki¹ , Einat Lev² , Janine Birnbaum² , and Jasper Baur² 

¹Graduate School of Environmental Studies, Nagoya University, Nagoya, Japan, ²Lamont-Doherty Earth Observatory, Columbia University, Palisades, NY, USA

Abstract Most lava flows carry bubbles and crystals in suspension. From earlier works, it is known that spherical bubbles increase the effective viscosity while bubbles deformed by rapid flow decrease it. Changes in the spatial distribution of bubbles can lead to variable rheology and flow localization and thus modify the resulting lava flow structure and morphology. To understand the roles of bubble and solid phase crystal distributions, we conducted a series of analog experiments of high bubble fraction suspensions. We poured the analog lava on an inclined slope, observed its shape, calculated the velocity field, and monitored its local thickness. A region of localized rapid flow and low vesicularity, whose thickness is thinner than the surrounding area, develops at the center of the bubbly flows. These features suggest that the locally higher liquid fraction decreases the effective viscosity, increases the fluid density, and accelerates the flow. We also found that a halted particle-bearing bubbly flow can resume flowing. We interpret this to result from the upward vertical separation of bubbles, which generates a liquid-rich layer at the bottom of the flow. In our experiment, bubbles are basically spherical and decrease the flow velocity, while our estimate suggests that bubbles in natural lava flows could increase or decrease flow velocity. Downstream decreases in flow velocity stops the bubble deformation and can cause a sudden increase of effective viscosity. The vertical segregation of the liquid phase at the slowed flow front may be a way to generate a cavernous shelly pahoehoe.

Plain Language Summary Lava flows can cover large areas and pose a hazard to buildings and infrastructure. To assess this hazard, we need to know what determines the shape and velocity of the lava flow. Most lava flows include bubbles, which can decelerate and accelerate lava flows depending on the bubble size and the flow velocity. Thus, heterogeneous bubble distribution may affect the lava flow shape and velocity. We simulated a lava flow by pouring a bubbly syrup as a lava analog on an inclined slope. We found that a more bubbly region flows slowly. The buoyant bubbles concentrate at the top of the flow front, while the liquid-rich layer generated at the bottom by vertical bubble separation lubricates the bottom boundary. These results show that bubble localization within a lava flow can be a source of variations of shape and velocity in natural lava flows. In the field, we sometimes find a cavernous structure beneath a solidified lava surface, which can be as large as a meter size, known as shelly pahoehoe. Our experiments suggest that such hollow voids may be generated by bubble accumulation at the top of the flow front.

1. Introduction

Basaltic eruptions can produce voluminous lava flows which cover large areas and pose a hazard to infrastructure and private property (Jenkins et al., 2017; Neal et al., 2019). Forecasting the direction and velocity of lava flows is essential for properly mitigating volcanic hazard (Chevrel et al., 2021; Dieterich et al., 2015; Fujita et al., 2009). Accurate prediction of flow direction and velocity is challenging because lava flows are sensitive to initial eruption conditions, interactions with the surrounding terrain and environment, and changes in the lava properties (Biass et al., 2019; Rumpf et al., 2018). The velocity and morphology of lava flows depend on the complex rheology of magmas and flow conditions (deGraffenried et al., 2021; Fink & Griffiths, 1990; Gregg & Fink, 2000; Griffiths, 2000; Harris & Rowland, 2001; Katz & Cashman, 2003; Kerr et al., 2006; Lev et al., 2012; Richardson & Karlstrom, 2019; Stasiuk et al., 1993).

Magma rheology is strongly modulated by the chemical composition, volatile content, temperature, and the presence of suspended bubble and crystal phases, all of which can change the viscosity by several orders of magnitude (Di Fiore et al., 2021; Kolzenburg et al., 2018; Leshner & Spera, 2015; Mader et al., 2013; Moitra & Gonnermann, 2015; Soldati et al., 2021). Lava flows frequently include bubbles and crystals. Vesicularity, i.e.,



Figure 1. A photograph of solidified shelly paho'eho'e from the Kilauea 2018 LERZ eruption found 16 m from the edge of the lava flow channel at 19.46386°N, 154.91011°W. The scale length is 1 m.

volume fraction of solidified bubbles, in natural flows varies in wide range, e.g., 0.02–0.88 at Kilauea and 0.04–0.71 at Etna (Cashman et al., 1994; Chevrel et al., 2018; Gaonac'h et al., 1996; Halverson et al., 2021; Harris & Rowland, 2015; Herd & Pinkerton, 1997; Patrick et al., 2019). Higher vesicularity is measured close to the vent and decreases with flow distance (Cashman et al., 1994). Bubble coalescence in a highly vesicular paho'eho'e lava flow generates various void structures (Walker, 1989). Crystal content in lavas at Kilauea is 0.05–0.35 (Gansecki et al., 2019; Robert et al., 2014). In addition, magmas and lavas can have strain-rate dependent behavior which can have important consequences on flow dynamics, e.g., by causing the transition from paho'eho'e to 'a'a (Sehlke et al., 2014).

As a fluid dynamics problem, the morphology and velocity of viscous flow on a slope have been investigated extensively theoretically and experimentally (e.g., Craster & Matar, 2009; Didden & Maxworthy, 1982; Huppert, 1982b; Mériaux et al., 2022). An analytical solution for a viscous flow on a sloping plane predicts that the flow length increases with time according to a power-law relationship (Lister, 1992), whose power index depends on the fluid's rheological properties (Balmforth et al., 2007).

Bubbles in magma can increase or decrease the effective viscosity depending on whether bubbles can deform under a certain shear rate (Llewellyn & Manga, 2005; Manga et al., 1998). Large-scale lava flow experiments using molten basalt have shown that bubbles increase the effective viscosity (Soldati et al., 2020), while field measurements of viscosity at high shear rate suggest the decrease of effective viscosity (Chevrel et al., 2018, 2019). We discuss this in detail in Sections 2 and 6.

Bubbles and crystals can also sometimes cause a yield strength, a minimum stress required to allow deformation. If the stress caused by the weight of the fluid layer does not exceed the yield strength, it will not flow. Here, the yield stress is mostly due to the microstructure of the suspensions, which can evolve with time. In a fluid layer slightly overcoming the yield strength, a slow downflow changes the microstructure in suspension, decreases the viscosity, and then accelerates the gravity flow (Coussot et al., 2002). Later injection of the low particle fraction fluid causes acceleration of the flow (Castruccio et al., 2014). Yield stress fluids show shear localization even in homogeneous stress fields (Møller et al., 2008). The yield strength and fluid properties depend not only on the particle volume fraction but also on the particle size distribution (Castruccio et al., 2010).

The shear conditions and phase concentrations, and therefore rheology, of lava flows can vary greatly in space and time during an eruption. For example, the voluminous lava flow eruption in 2018 at the lower East Rift Zone (LERZ) of Kilauea Volcano, Hawai'i, exhibited rapid flow with velocities up to 15 m s^{-1} within the confined channel (Dietterich et al., 2021; Patrick et al., 2019). Yet overflowed lava from the channel showed slow and thin patches. Such a significant change of lava behavior only a short distance from the source is different from previously observed lava flows (Biass et al., 2019).

At the flow front of some thin overflows, the lava formed large cavities with a length scale of $>1 \text{ m}$ inside the closed flow patch, called shelly paho'eho'e (Jones, 1943; Swanson, 1973; Wentworth & Macdonald, 1953). Figure 1 shows a photograph of a solidified shelly paho'eho'e formed during the 2018 eruption at the lower East Rift Zone (LERZ) of Kilauea Volcano, Hawai'i. The standard explanation for forming such cavities is an emptying out of the lava beneath a solidified crust, similar to a small lava tube. However, this flow patch, and others like it, do not have an outlet through which to discharge the lava (Figure 1). This feature requires an alternative mechanism for formation in which gas accumulates at the toe of the flow. Here, we propose a formation mechanism through a process of flow localization and large bubble concentration at the flow front. We investigate this mechanism, and the behavior of highly vesicular flows in general, through a series of experiments with bubbly lava flow analogs.

2. Rheology of a Complex Multiphase Fluid

Bubbles and particles in fluid suspensions change the effective viscosity of suspensions, relative to that of the liquid phase, η_l . We here define the bubble volume fraction ϕ_b and the particle volume fraction ϕ_p as

$$\phi_b = \frac{V_b}{V_l + V_b + V_p} \quad (1)$$

$$\phi_p = \frac{V_p}{V_l + V_p} \quad (2)$$

where V_l , V_b , and V_p are the liquid, bubble, and particle volumes, respectively. We define the particle volume fraction with respect to the dense rock equivalent (bubble-free) suspension to be consistent with the literature (e.g., Chevrel et al., 2018; Gurioli et al., 2014).

2.1. The Effect of Particles

The effective viscosity of a liquid-particle flow increases with the particle volume fraction. One such model expresses the viscosity ratio η_r as

$$\eta_r = \frac{\eta_{\text{eff}}}{\eta_l} = \left(1 - \frac{\phi_p}{\phi_{\text{max}}}\right)^{-C\phi_{\text{max}}} \quad (3)$$

where η_{eff} is the effective viscosity of the particle-bearing fluid, ϕ_p is the volume fraction of particles, and ϕ_{max} is the maximum possible volume fraction of particles or undeformed bubbles in random close packing, and the exponent is $2.0 \leq C\phi_{\text{max}} \leq 2.5$ (Mader et al., 2013). The random close packing of spheres of uniform size is $\phi_{\text{max}} = 0.64$. This value decreases with increasing particle aspect ratio and increases with increasing size variation (Klein et al., 2017; Mueller et al., 2011). An alternative view of the particle size contribution is that the small particles together with the liquid phase form a viscous fluid phase, and the large particles determine the solid fraction in Equation 3 (Castruccio et al., 2010).

2.2. The Effect of Bubbles

The effective viscosity of bubbly fluids depends on the capillary number (Llewellyn et al., 2002; Manga & Loewenberg, 2001; Pal, 2003), which is a measure of whether the bubbles will get deformed by the flow. It is defined as the ratio of viscous stresses acting to deform bubbles, and surface tension resisting deformation

$$\text{Ca} = \frac{\eta \dot{\gamma} R}{\Gamma} \quad (4)$$

where $\dot{\gamma}$ is strain rate, R is the bubble radius, and Γ is the surface tension. In this equation, the viscosity η can be either the effective viscosity η_{eff} or liquid viscosity η_l . When a large bubble is surrounded by a suspension with smaller bubbles and particles, the dominant viscous force for the deformation of the bubbles depends on the effective viscosity η_{eff} . In contrast, the viscous force to deform an isolated bubble should be defined with the liquid viscosity η_l . For $\text{Ca} < 1$, bubbles do not deform and behave similarly to solid particles, thus increasing the effective viscosity as is expected by Equation 3 by replacing ϕ_p to the volume fraction of bubble ϕ_b . In this case, ϕ_{max} in Equation 3 becomes the random close packing of undeformed bubbles, and for monodisperse bubbles $\phi_{\text{max}} \sim \phi_{\text{bmax}} \sim 0.64$. Again, ϕ_{bmax} is sensitive to the bubble size distribution.

For $\text{Ca} > 1$, bubble deformation becomes significant and decreases the effective viscosity. Some theoretical and empirical equations have been suggested for the impact of bubbles on the effective viscosity for different Ca regimes. A numerical estimate of the relative viscosity for an infinite shear rate (high Ca) is close to the Hashin-Shtrikman upper bound (Manga & Loewenberg, 2001)

$$\eta_r = \frac{\eta_{\text{eff}}}{\eta_l} = 1 - \frac{5\phi_b}{3 + 2\phi_b} \quad (5)$$

Pal (2003) formulated the relative viscosity at an infinite shear rate as

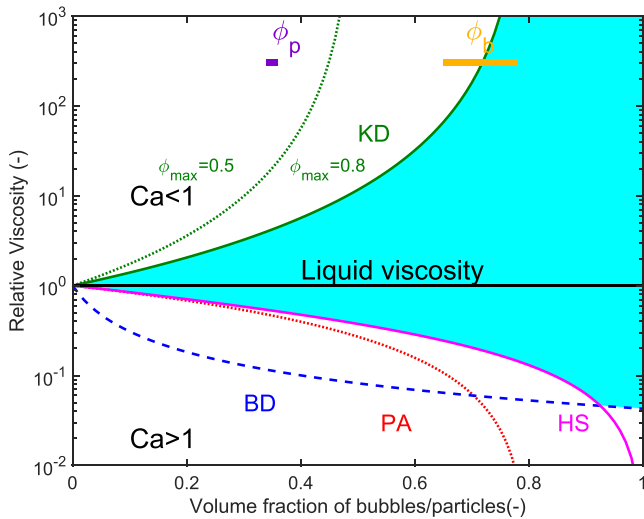


Figure 2. Summary of the effective viscosity model. The curves labeled KD, HS, PA, and BD are defined by equations of 3, 5, 6, and 7, respectively. We assumed $\phi_{\max} = 0.5, 0.8$, $C\phi_{\max} = 2.5$, in Equation 3, and $\phi_{\text{bmax}} = 0.8$ in Equation 6. The horizontal bars indicate the fraction ranges of bubbles and particles in our experiments. The color indicates an approximately minimum variation of effective viscosity in this estimate.

$$\eta_r = \frac{\eta_{\text{eff}}}{\eta_l} = \left(1 - \frac{\phi_b}{\phi_{\text{bmax}}}\right)^{5\phi_{\text{bmax}}/3} \quad (6)$$

Bagdassarov and Dingwell (1992) suggested an empirical equation

$$\eta_r = \frac{\eta_{\text{eff}}}{\eta_l} = \frac{1}{1 + 22.4\phi_b} \quad (7)$$

Figure 2 summarizes these equations. The shaded area in light blue indicates the possible variation of the relative viscosity with or without bubble deformation, which can reach several orders of magnitude.

We here emphasize quantitative estimates of effective viscosity based on above models have limitations. Bubbles within a suspension can have significant size variation, increasing the maximum bubble fraction and modulation of effective viscosity for undeformed bubbles (Equation 3). Bubble size variation also alters the criteria of deformation through Ca (Equation 4). Temporally evolving bubble shape and size by coalescence can affect the effective viscosity of bubbly fluids (Takeda et al., 2020). A qualitatively meaningful interpretation of the above scalings is that bubbles can increase the effective viscosity by several orders of magnitude while decreasing it by only 1 order of magnitude (Figure 2).

Bubbles are deformable to be polyhedral so that the bubble fraction can exceed the random close packing of monodisperse spheres ($\phi_b > \phi_{\text{bmax}} = 0.64$). Such a bubbly fluid has elasticity by surface tension. An empirical relation describes the shear modulus as a function of the bubble radius and fraction (Hohler & Cohen-Addad, 2005)

$$G \sim \phi_b (\phi_b - \phi_{\text{bmax}}) \frac{\Gamma}{R} \quad (8)$$

Here, \sim indicates approximation in a factor.

For a rhyolitic magma, the effect of surface tension is negligible relative to the shear modulus of the liquid phase, the shear modulus decreases with bubble fraction

$$\frac{G}{G_0} \sim (1 - \phi_b)^\zeta \quad (9)$$

where G_0 is the shear modulus of bubble-free suspending fluid and $1 < \zeta < 4$ is constant (Namiki et al., 2020).

The yield stresses τ_y reported for foams by oscillatory measurements are approximately described by the following relation (Hohler & Cohen-Addad, 2005):

$$\tau_y = 0.5 \frac{\Gamma}{R} (\phi_b - \phi_{\text{bmax}})^2 \quad (10)$$

2.3. Three-Phase Effect

When both bubbles and particles exist in a suspending fluid and bubbles do not deform, the volume fraction of the deformable suspending fluid decreases. Thus, adding bubbles to a dilute particle suspension at the low capillarity number regime increases its viscosity. In contrast, adding bubbles to a concentrated particle suspension, where space of the deformation is limited, decreases its viscosity (Truby et al., 2015). An effect of high-volume fraction of particles on the behavior of bubbles has been experimentally confirmed (Pistone et al., 2016).

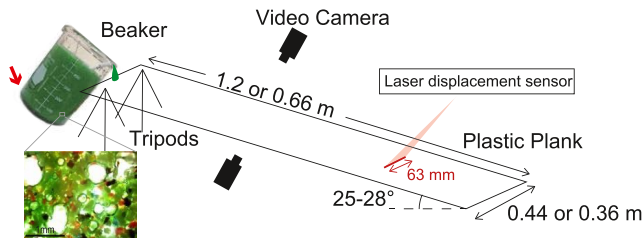


Figure 3. A schematic diagram of our apparatus. The inset figure shows the complex fluid image containing bubbles (white) and particles (black, red, and gray) in corn syrup (green) imaged under a microscope. This sample is a part of the fluid prepared as the analog material of lava flow, taken from the beaker and observed after the experiments. The suspension, which is opaque in 3D, is thinly stretched on a slide glass to be approximately 2D. On the slide glass, the bubbles are separated by long distances to prevent the bubble coalescence and coarsening.

The three-phase fluid also has elasticity. The shear modulus can be written by the product of bubble effect (Equation 8) and particle effect (Equation 3; Namiki & Tanaka, 2017)

$$G \sim \frac{\Gamma}{R} \phi_b (\phi_b - \phi_{bmax}) \left(1 - \frac{\phi_p}{\phi_{max}}\right)^{-C \phi_{max}} \quad (11)$$

Recall that Equation 3 accounts for reducing the viscously deformable space. Equation 11 has similar dependence on ϕ_p , suggesting a reduction of the elastically deformable space.

Birnbaum et al. (2021) developed a set of empirical expressions to describe the rheological parameters of three-phase suspensions with both particles and bubbles that is based on a Herschel-Bulkley formulation (Herschel & Bulkley, 1926)

$$\tau = \tau_y + K \dot{\gamma}^n \quad (12)$$

where τ is the shear stress, τ_y is the yield stress, K is the consistency, and n is the flow index ($n > 1$ implies shear-thickening, $n < 1$ shear-thinning). Using analog dam-break flow experiments in confined channels, the following expressions were derived:

$$\frac{K}{\eta_i} = \left(1 - \frac{\phi_p}{\phi_m}\right)^{-B_p} (1 - \phi_b)^{-B_b} \quad (13a)$$

$$\tau_y = 10^{C_1(\phi_p - \phi_{c,\tau_y})} + 10^{C_2(\phi_b + \phi_b - \phi_{c,\tau_y})} \quad (13b)$$

$$n = \begin{cases} 1, & \phi_b (1 - \phi_b) + \phi_b \leq \phi_{c,n} \\ 1 + (C_3 - C_4 Ca) (\phi_{c,n} - \phi_p (1 - \phi_b) - \phi_b), & \phi_b (1 - \phi_b) + \phi_b > \phi_{c,n} \end{cases} \quad (13c)$$

where $\phi_m = 0.56 \pm 0.20$, $B_p = 2.74 \pm 1.56$ and $B_b = 1.98 \pm 0.09$, $C_1 = 80.0 \pm 10.9$, $C_2 = 1.98 \pm 0.23$, the critical volume fraction for the onset of appreciable yield stress $\phi_{c,\tau_y} = 0.35 \pm 0.01$, $C_3 = 0.70 \pm 0.25$, $C_4 = 0.55 \pm 0.31$, and the critical volume fraction for the onset of shear rate dependence $\phi_{c,n} = 0.39 \pm 0.12$.

The common characteristic of the three-phase fluid is that the solid particles can increase viscosity and elasticity significantly, while the effects of bubble is limited (Birnbaum et al., 2021; Namiki & Tanaka, 2017; Truby et al., 2015).

3. Experimental Methods

To understand the effect of a high-volume fraction of bubbles and crystals on a lava flow, we conducted a series of experiments of a particle-bearing bubbly lava flow analog, made of corn syrup as the liquid phase, plastic particles as crystal analogs, and CO₂ bubbles. We simulated the lava flow by pouring the lava analog on an inclined acrylic plank (Figure 3). The experimental conditions are summarized in Table 1.

To create our lava analog, we mixed corn syrup and plastic particles in a beaker until the mixture was uniform and then added reactants into the mixture. The chemical reaction caused a volume increase of the mixed suspension. The corn syrup had a temperature and water-content dependent viscosity (Figure S1 in Supporting Information S1) that we varied between 0.35 and 150 Pa s and surface tension of 0.08 N m⁻¹ (Rust & Manga, 2002). We conducted all experiments at the same room temperature so that the temperature-dependence of the syrup viscosity did not impact the results. We present the water-content dependence at the same temperature in Figure S1 in Supporting Information S1). The plastic particles had a density in a range of 1,400–1,500 kg m⁻³, were irregularly shaped with an aspect ratio of 1.5 and 0.1 mm in size in averages, and served as analogs to crystals.

We introduced bubbles by a chemical reaction of baking soda and citric acid, which generated CO₂. This is the same technique and materials used in previous works (Birnbaum et al., 2021; Namiki & Tanaka, 2017).

Table 1
Experimental Conditions

	Slope	Plank length	Liquid viscosity	Liquid density	Total volume	ϕ_b	ϕ_p
	(°)	(m)	(Pa s)	(kg m ⁻³)	(L)	(-)	(-)
Figure 4a	28	1.2	0.35	1,315	0.44	0.00	0.00
Figures 4b and 6b	28	1.2	0.35	1,315	0.43	0.69	0.00
Figures 4c and 6c	28	1.2	0.35	1,315	0.42	0.69	0.35
Figure 6a	25	0.66	150	1,470	0.50	0.00	0.00
Figure 6d	26	0.66	1.9	1,370	0.38	0.65	0.00
Figure 7	25	0.66	1.0	1,350	0.10	0.78	0.00

Note. Total volume is the poured volume on the plank for the model lava flow.

The amount of bubbles could be roughly controlled by adjusting the amount of baking soda and citric acid. However, the gas produced could not be finely controlled because it escapes into the atmosphere during the reaction. The bubble volume was calculated by subtracting the volume of liquid and particles from the total volume of the suspension. We measured the total volume of the three-phase suspension using a graduated beaker. By introducing bubbles, the liquid color became whitish, indicating that the fluid color can be a measure of bubble fraction. The liquid and particle volumes were calculated by their mass and density. The vesicularity range used in our experiment was 0.65–0.78, which simulated the highly vesicular lava flow (0.5–0.82) that erupted during the 2018 LERZ eruption from Ahu'a'ilā'au (formerly known as Fissure 8) at Kīlauea Volcano, Hawai'i (Patrick et al., 2019; Figure 1). Crystallinity in lavas from Ahu'a'ilā'au is low (0.05), while that for the early phase is 0.35 (Gansecki et al., 2019). The particle fraction in our experiments simulated the latter case.

After the volume increase stopped and before any significant liquid separation from the foam by gravity occurs, we poured the fluid from the beaker by hand onto a plastic plank, inclined at angles of 25–28° from horizontal. This slope angle was chosen to be consistent with conditions in nature and allow measurements of active flow with the given materials. We tried slopes from 8° to 45° and found that a flow on a steeper slope lengthens in the direction of the downslope, while a flow on a shallow slope acquires a round shape. We also found a technical problem that the flow down a shallow slope of <20° is too slow, and its surface dried during the experiment due to water evaporation. A very steep slope >30° is rare in nature (Biass et al., 2019; Favalli et al., 2010).

The duration of pouring was on the order of 10 s. We tried various methods of introducing the particle-bearing bubbly mixture onto the plank, such as injection through a tube or removal of a dam, and found that controlling the flow rate of the non-Newtonian sticky fluid was quite difficult. In addition, flow in a tube modified the bubble fraction in the fluid before it reached the plank. We thus concluded that this simple method of pouring directly from a beaker is the best way as a first step to simulate short lived unconfined bubbly lava flows.

We observed the analog lava flow on the transparent acrylic plank using video cameras, and quantified the velocity field at the surface on the videos using optical flow velocimetry (Lev et al., 2012; Sun et al., 2010). For the measurement of the velocity field of pure liquid flow, we used a more viscous fluid than that of the reference experiment. This was because to measure the velocity field for a pure liquid, we needed to add tracers on the flow surface. Adding tracers to the rapid flow with low viscosity is challenging. Note that the appearance of two pure liquid flows was similar in terms of no localized flow. In some experiments, we used a laser displacement sensor (Omron ZG2, vertical resolution of 6 μm) to measure the surface topography of the flow. We also used a more viscous liquid for topography measurement. The surface of the bubbly flow with lower viscosity liquid had more large bubbles, which became scattering sources of the laser beam. We calculated the time evolution of the topography at two representative locations from the line sensor output. Characteristics of bubbles can vary with time and space, which cannot be monitored quantitatively. In this series of experiments, we thus try to understand the bubbly flow in a qualitative manner.

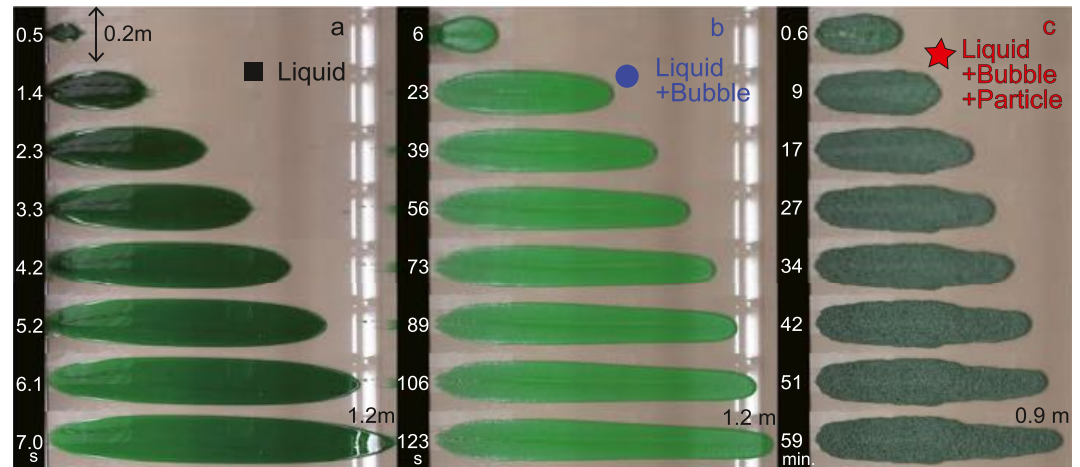


Figure 4. Photographs of the lava flow experiments with (a) pure liquid, (b) bubbly flow $\phi_b = 0.69$, and (c) particle-bearing bubbly flow $\phi_b = 0.69$ and $\phi_p = 0.35$. The conditions are summarized in Table 1. The liquid viscosity $\eta_l = 0.35$ Pa s is the same for three experiments. The markers correspond to Figure 5. The numbers denoted on the left side show the elapsed time since the front of the pouring fluid contacts the plank. The length of the lava flow in the last photograph is denoted at the bottom. The width of each panel is 0.2 m. The light-colored vertical lines are the reflection of overhead fluorescent lights. The corresponding movie is provided as Movie S1, which is introduced in Gasparini (2020).

We can estimate the yield stresses for our bubbly lava analog. According to Equation 10, the yield stress for bubbly fluid depends on the maximum bubble volume fraction. Assuming $\phi_{bmax} = 0.64$, our bubbly fluid with $\phi_b \leq 0.78$ and bubble size of $>10^{-4}$ m has yield stress of <10 Pa. Using Equation 8, the shear modulus is <100 Pa, resulting in that the critical strain for yield becomes <0.01 . Similarly, the yield stress for our three-phase suspension is estimated using Equations 13b, 24 Pa, and the shear modulus is 200 Pa (Equation 11), resulting in the critical strain for yielding of 0.1. Note that the characteristics of the three-phase fluid, such as liquid surface tension and particle size, can affect also the yield stress. The fluid used by Birnbaum et al. (2021) to derive Equation 13b was approximately the same as that in this paper.

4. Results

4.1. Flow Velocity Slowed by Bubbles and Particles

Figure 4 summarizes three typical experiments. We used three kinds of fluids; pure liquid, bubbly fluid, and particle-bearing bubbly fluid. The most significant result is that the pure liquid flows rapidly, while the bubbly fluid and the particle-bearing bubbly fluid flow slowly. At the downslope nose of the pure liquid, droplets originating from capillary instability precede the flow (Figure S2 in Supporting Information S1; Huppert, 1982a; Lister, 1992).

To visualize this trend quantitatively, we plot the time evolution of the length of each flow (Figure 5a). Theoretically, the length of flows would be expected to increase with time t in a power-law manner t^α —for a Newtonian fluid, while the fluid is being poured at a constant flux, $\alpha = \frac{7}{9}$, and after the pouring ends, $\alpha = \frac{1}{3}$, as denoted in Figure 5a (Lister, 1992).

The pure liquid, expected to behave as a Newtonian fluid, flows down rapidly and the flow length time evolution follows the power index of $\frac{7}{9}$, as expected for a Newtonian fluid. This result suggests that the flux rate we achieve by pouring is nearly constant, despite pouring by hand. Given that the flow is too rapid, the flow front reaches the bottom end of the plank before the pouring ends, and we could not obtain the power index of length evolution after the pouring ends (Figures 4a and 5a).

In contrast, the flow of the bubbly fluid advanced much more slowly than the pure liquid (Figure 4b). Bubbly fluids are often non-Newtonian, and advance according to different power-law indexes (Balmforth et al., 2007; Birnbaum et al., 2021). In our experiment for bubbly fluids, the power-law index before the end of pouring deviates from the $\alpha = \frac{7}{9}$ expected for Newtonian fluids. This may suggest the effect of non-Newtonian rheology, but

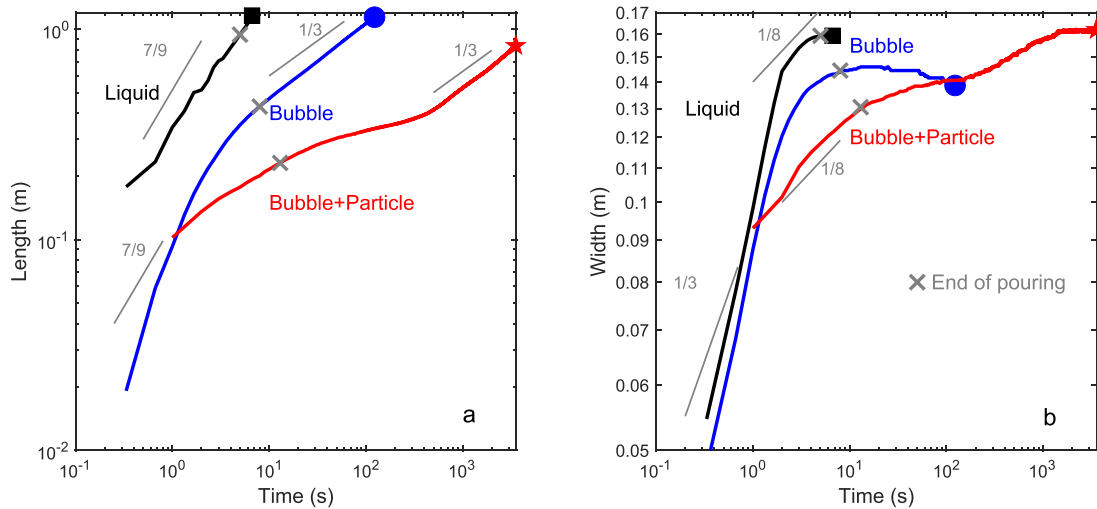


Figure 5. The time evolution of (a) the length and (b) the maximum width of the lava flows observed in Figure 4. The theoretically predicted power indexes for Newtonian fluids are denoted as gray lines. The flow shape is extracted from the top view video (Figure 4) using color contrast, which can produce an error of a few pixels, <5 mm.

because of short time pouring different from Balmforth et al. (2007), the power index until the end of pouring does not reach a constant. Once the pouring stopped, though, the flow advance rate follows a power-law index of $\frac{1}{3}$, which is consistent with a Newtonian behavior (Figure 5a).

The behavior of the particle-bearing bubbly fluid is more complex. The time evolution of the length approximately stops around 100 s, but the fluid resumes to flow down around 500 s at a rate following a power-law index of $\frac{1}{3}$, consistent with Newtonian behavior. In Figure 4c at 17 min, the width of the flow front is narrower than that of the original, indicating that the former entire flow upslope adheres to the plank and only the central part of the flow is mobile. The width of the flow front decreases with time. The low power index before reaching $\alpha = \frac{1}{3}$ may be due to the rheology effects such as yield stress and shear rate dependence (Balmforth et al., 2007; Birnbaum et al., 2021). The time varying power index may suggest that these rheological parameters are also time dependent.

The maximum widths of these three examples do not differ significantly (Figure 5b). The bubbly fluid shows a slight decrease in measured maximum width with time after the pouring end. This is because the fluid upslope at the maximum width flows down to make the measured width narrower. In addition, some bubbles at the edge of the flow disappear with time. The width of particle-bearing bubbly suspension continuously increases for a long time. This is because the initially thick flow spreads by gravity in both the downslope and cross-slope directions.

The width of flows is also expected to increase over time in a power-law manner, t^α . For a Newtonian fluid, while the fluid is being poured at a constant flux, $\alpha = \frac{1}{3}$, and after the pouring ends, the growth stops and $\alpha = 0$ (Lister, 1992). In Figure 5b, the initial phase is faster than $\alpha = \frac{1}{3}$, which may originate from the width of the beaker, which is wider than a point source. The later stage of pouring is close to $\alpha = \frac{1}{8}$. The power index of $\frac{1}{8}$ is derived, assuming that fluid flux is approximately zero at the very beginning of pouring. Maybe our hand moved downslope. This should halt the width evolution at a certain location but not much affect the evolution in length.

4.2. Spatial Variation of Velocity and Thickness

In bubbly fluid experiments (Movie S1, Figure 4b), a dark linear structure appears along the center axis at the end of the pouring, which overtakes the other whitish parts downslope. Here, the dark fluid color is due to fewer bubbles, implying that this region is denser than the surrounding whitish region. We here quantify this feature by measuring the flows' surface velocity field (Figures 6a–6c) and flow thickness (Figure 6d). Figures 6b and 6c is

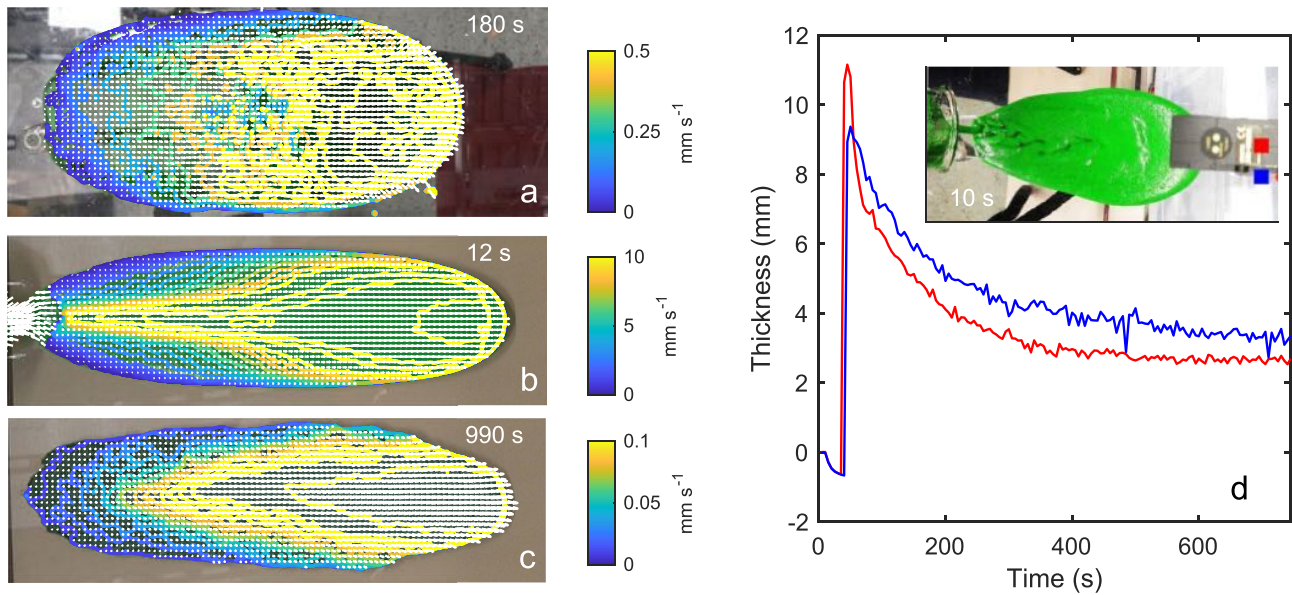


Figure 6. The calculated velocity field for (a) pure liquid with a viscosity of 150 Pa s, (b) bubbly fluid (Figure 4b), and (c) particle-bearing bubbly fluid (Figure 4c). The length of each panel is 0.6 m. The contour curves show the velocity in the downslope direction, and arrows show the flow direction with a velocity scaled to relative magnitude. The numbers indicate the time after pouring. Corresponding movies are provided as Movies S2–S4. (d) Measured flow thickness for the bubbly fluid with a liquid viscosity of 1.9 Pa s and the bubble fraction of 0.65. Measured locations of red and blue curves are marked at the inset. One in the channel center and one offset by 37 mm, both 0.35 m downslope from the initial pouring location. The area of the inset is 0.45×0.2 m.

the velocity field of Figures 4b and 4c, and Figure 6a is the velocity field of pure liquid flow with more viscous fluid than that used in Figure 4a.

Figures 6a–6c show that the flow front has higher velocity than upslope. The pure liquid flow, as a Newtonian fluid, has a limited velocity variation in the cross-slope direction (Figure 6a), while the bubbly fluid shows strongly localized flow (Figure 6b). This region corresponds to the dark linear structure, indicating that the dense region with fewer bubbles flows faster than the surrounding. The particle-bearing bubbly flow shows that the flow is concentrated in the narrow flow front, which corresponds to the region that resumed motion after coming to a near halt (Figure 6c).

Motivated by the importance of thickness on flow velocity, we then measured the flow thickness using a laser displacement sensor (Figure 6d). The liquid viscosity in Figure 6d is higher than that used in Figure 4b, and bubbles in both Figures 4b and 6d maintain spherical shapes, suggesting that $Ca < 1$. The inset shows a photo of the measured flow, in which darker spots appear at the middle of the flow. These darker spots, together with the whitish region between them, rapidly flow down. Initially, the flow front is upslope of the sensor. After 40 s, the flow front reaches the location of the sensor (Figure 6d). As expected, the flow front is relatively thick, and the height decreases with time as the flow is advected downslope. So, the x -axis time in Figure 6d can be considered as the distance from the flow front. The center of the flow (red curve) is thicker than the side (blue curve) at the flow front, but later the side becomes thicker than the center.

4.3. Observation From Underneath the Plank

When we made the bubbly fluid in the beaker, the liquid was segregated by gravity and formed a lower liquid layer with dark color (Figure 3, red arrow). This process may also be important in the flow. We then observed the bubbly flow from the bottom of the plank (Figure 7). The bottom view shows a darker color, suggesting that more liquid accumulates at the bottom of the flow. The bottom view also shows that, as the experiment progresses, the darker region concentrates at the flow front. The side view indicates the flow front is thicker than the upslope region. The top view shows an increased concentration of bubbles at the flow front.

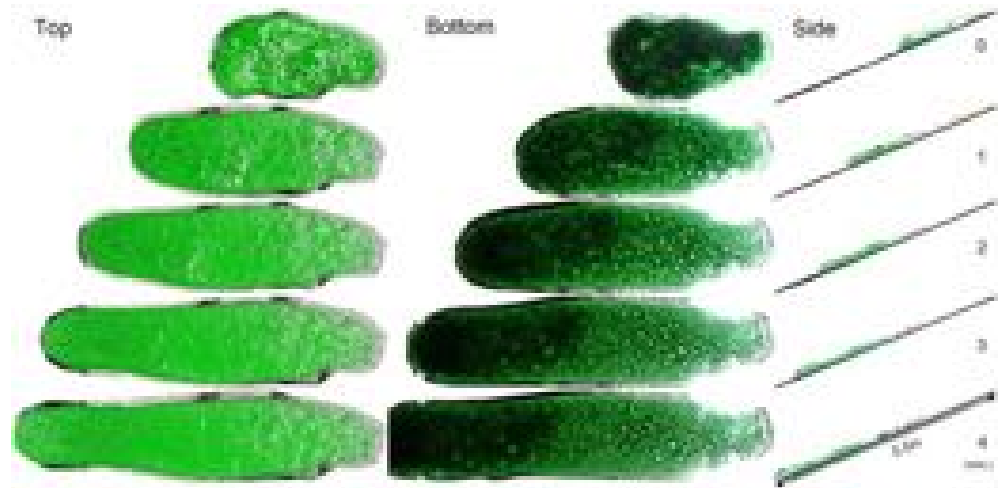


Figure 7. An example observation from three directions of a bubbly flow with liquid viscosity of 1 Pa s and bubble fraction of 0.78. The length of each panel is 0.5 m. The panels show top, bottom, and side views from the left. Please note that the flow direction is from right to left to be consistent with the side view. We painted the noisy background with white and remained the rim of fluids to avoid the artificial effect.

5. Discussion

5.1. Why Did Bubbles Only Slow the Flows?

Our experiments show that the bubbly flow is slower than the pure liquid flow for the same liquid viscosity. Recall from Section 2 and Figure 2, bubbles can increase or decrease the effective viscosity. Because, in our experiments, bubbles only slowed the flow velocity, we infer that the bubbles did not substantially deform.

To confirm this hypothesis, we estimate the capillary number for our bubbly fluid flow. The vertically averaged mean flow velocity in the layer u for a Newtonian fluid on a slope angle of θ is calculated by (Turcotte & Schubert, 2014)

$$u = \frac{\rho g h^2 \sin \theta}{3\eta_{\text{eff}}} \quad (14)$$

where $\rho = \rho_l(1 - \phi_b)$ is the effective density of the fluid, $g = 9.8 \text{ m s}^{-2}$ is the gravitational acceleration, h is the thickness of the flow. Equation 14 gives a simple order of magnitude estimate of velocity, which in reality varies throughout the flow depth and with any spatial or temporal variations in the flow. Indeed, our experiments show that the flow thickness and bubble distribution vary locally and temporally (Figures 6 and 7). In a natural lava flow, the slope angle also differs locally. We regard Equation 14 as applicable for the local average in a relatively homogeneous region.

We take the average shear rate $\dot{\gamma}$ in the definition of Ca (Equation 4) to be u/h . Substituting Equation 14 and this definition of $\dot{\gamma}$ into Equation 4, the viscosity term disappears and we obtain

$$\text{Ca} = \frac{\rho_l(1 - \phi_b) g h R \sin \theta}{3\Gamma} \quad (15)$$

In this equation, the liquid density, surface tension, and slope angle do not vary significantly. That is, the flow thickness and bubble size are the dominant factors determining the capillary number. In our experiments, the flow thickness varies temporally and locally and is on the order of 10^{-2} m (Figure 6d). The bubble sizes also vary in the range of 10^{-4} – 10^{-2} m. The minimum size of 10^{-4} m is measured under microscope (Figure 3), and the maximum is measured from videos of analog lava flow, taking the time variation into account (Figures 4 and 7).

We plot Equation 15 in Figure 8 and find that the possible bubble radius and flow thickness range in our experiments are located in the field of $\text{Ca} < 1$, indicating that the bubbles do not deform and effective viscosity increases. This estimate is consistent with our observation that the bubbles always slow the flow velocity.

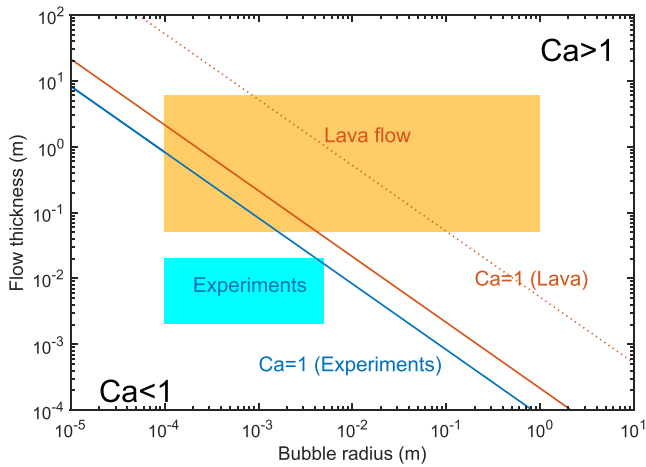


Figure 8. The estimated capillary number depending on the flow thickness and bubble radius (Equation 15). The red and blue lines indicate $Ca = 1$ for a lava flow and model lava flow in our experiments, respectively. The orange and blue area indicates a possible range of real lava flow and model lava flow, respectively. We here assume $\rho_l = 2,700 \text{ kg m}^{-3}$, $\theta = 25^\circ$ (solid line), $\theta = 1^\circ$ (dotted line), $\Gamma = 0.4 \text{ N m}^{-1}$ for a lava flow, and $\rho_l = 1,400 \text{ kg m}^{-3}$, $\theta = 25^\circ$, $\Gamma = 0.08 \text{ N m}^{-1}$ for experiments. For lava flow, the range of thickness and slope is estimated by the eruptions at Kilauea (Biass et al., 2019; Dietterich et al., 2021; Patrick et al., 2019) and Mt. Etna (Favalli et al., 2010). The bubble size is based on the field observations (Chevrel et al., 2018; deGraffenried et al., 2021; Shea et al., 2010; Figure 1). For experiments, the range of the flow thickness is estimated based on the side view (Figure 7) and the measurement by the laser displacement sensor (Figure 6). The bubble radius range is estimated by the analog lava flow video and microscope measurements (Figures 3, 4, and 7).

We here note that Equation 15 assumes that a large bubble is surrounded by bubbly fluid. When ϕ_b is small or bubble size is uniform, liquid viscosity may be more appropriate to be a substitute in Equation 4. Given that most bubbles did not deform in our experiments Equation 15 becomes

$$Ca = \frac{\rho_l (1 - \phi_b) g h R \sin \theta}{3\Gamma} \left(1 - \frac{\phi_b}{\phi_{\max}}\right)^{C\phi_{\max}} \quad (16)$$

The last term decreases with increasing ϕ_b to reduce Ca . Thus, estimated Ca in Figure 8 is the maximum estimate. Again, our experiments are located in the field of $Ca < 1$ irrespective of the surrounding fluid properties.

5.2. Flow Localization and Vertical Segregation of Liquid

5.2.1. Summary of Observation

In Section 4.2, we quantified the characteristics of flow localization. In the bubbly flow, the line-like dark region has a thinner thickness and flows faster than the surrounding region (Figures 6b and 6d). To understand the source of this structure, we revisit the initial condition. When we made the bubbly fluid in the beaker, the lower part of the beaker became relatively liquid-rich by gravitational segregation (Figure 3, red arrow). As a result, when we poured the bubbly suspension on the plank from the beaker, the fluid that came out later had fewer bubbles. Since the driving force of the downslope flow is gravity, this later fluid parcel, which has fewer bubbles and thus a higher bulk density and lower effective viscosity, flows down faster than the surrounding fluid and becomes thinner. These characteristics are consistent with those observed in Figures 6b and 6d. We thus interpret this region to have a lower bubble fraction, originating from liquid separation in the beaker. Indeed, Movie S1 shows that the line-like dark structure appears at the end of the pouring. Our interpretation is consistent with the previous work in which later injected less viscous fluid accelerates the flow (Castruccio et al., 2014).

Such an artificial bubble distribution does not occur in nature. However, the temporal fluctuation of bubble fraction in an erupted lava has been observed during the LERZ eruption (Patrick et al., 2019). The above result indicates the importance of the heterogeneous bubble distribution in the gravitationally driven downflow. Next, we consider the effect of the vertical localization of bubbles, which may occur in natural systems.

In experiments with particle-bearing suspensions (Figure 4c), the flow resumed after almost stopping. It is known that suspension fluids with yield stress begin to flow abruptly once a threshold stress is overcome (Coussot et al., 2002). This is because the rheology depends on the internal microstructure and deformation fluidizes the jammed suspension to accelerate the flow.

The estimated yield stress for our particle-bearing bubbly fluid is 24 Pa (Equation 13b), which is close to the stress caused by the fluidal static pressure acting on the fluid layer $\rho_l(1 - \phi_b)gh \sin \theta \sim 20 \text{ Pa}$ with a thickness of $h \sim 10^{-2} \text{ m}$. This agreement explains the observation that the particle-bearing bubbly flow almost stops (Figure 5a, red curve, 100 s). The fluid was initially thick and generated the stress exceeding the yield stress $\rho_l(1 - \phi_b)gh \sin \theta > \tau_y$. With time, the fluid becomes thinner by flowing, and the stress acting on the flow falls below the yield stress, and then the flow stops. From our visual observation, it is not plausible that the critical strain of 0.1 for yielding occurs within the three-phase suspension to resume the downflow after the stopping. However, the flow resumed.

In contrast, the yield stress of the bubbly fluid of $< 10 \text{ Pa}$ is much smaller than the fluidal static pressure, which is consistent with the observation that the bubbly flow did not stop (Figure 4b). Irrespective of differences in yield stress, both flow lengths had the same power index of $\alpha = \frac{1}{3}$ close to that typical of a Newtonian fluid at the very end of observations (Figure 5a).

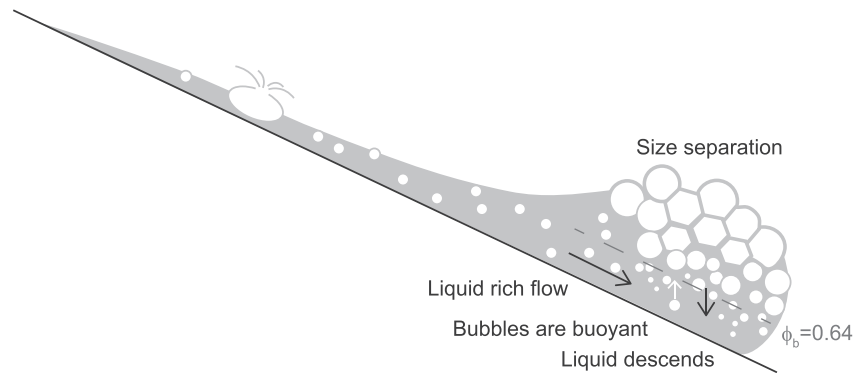


Figure 9. A schematic vertical cross-section of our analog lava flow. Liquid segregates from the bubbles generating a liquid-rich bottom layer, which lubricates the bottom of the bubbly flow. Bubbles accumulate above it.

We interpret this phenomenon as the result of vertical bubble localization developed with time. Less dense bubbles are buoyant in a bubbly suspension, and bubbles and liquid separate by gravity with time. Indeed, Figure 7 shows that the liquid in the bubbly flow concentrates at the bottom of the flow. Bubbles floated by buoyancy, and the liquid segregated to accumulate at the bottom.

5.2.2. Time Scale of Vertical Bubble Separation

Summarizing the above discussion, we interpret our experiments as shown in Figure 9. Liquid concentrates at the bottom of the flow front above which the bubbles float. The observation that our experiments approach the Newtonian scaling with time suggests that the bubble-poor regions at the base and center of the flow control the velocity of flow front propagation. Based on this idea, we estimate the time scale of vertical bubble separation.

The density contrast between liquid and bubble causes bubble floating and liquid drainage. We here focus on the two-phase system of bubble and liquid for simplicity. When the bubble fraction is lower than the random close packing $\phi_b < \phi_{max}$, the evolution of liquid-rich layer (dashed line in Figure 9) is produced by the floating of bubbles.

An isolated bubble in a liquid layer ascends under the balance of buoyancy and viscous drag which is known as Stokes velocity (Turcotte & Schubert, 2014)

$$u_{stk} = \frac{\rho_l g R^2}{3\eta_l} \quad (17)$$

In a suspension, the ascending of individual bubbles will be hindered by the presence of neighboring bubbles. This effect is empirically tested with settling particles (Davis & Birdsell, 1988). Applying this relation for bubbles, the hindered rise velocity becomes

$$v_h = (1 - \phi_b)^5 u_{stk} \quad (18)$$

Actual growth rate of the liquid-rich layer may be intermediate of Equations 17 and 18. This is because, in the experiment on gravity-driven settling of packed particles into a liquid layer, the growth rate of the liquid-rich layer is intermediate between velocities estimated by these two equations (Shibano et al., 2012).

Another way to estimate the liquid separation is using Darcy velocity, in which liquid phase flows down in the suspension

$$v_D = \frac{R^2(1 - \phi_b)^3}{45\phi_b^2} \frac{\rho_l \phi_b g}{\eta_l} = \frac{(1 - \phi_b)^3}{15\phi_b} u_{stk} \quad (19)$$

where we assumed that pressure difference is originated from the density difference of mixture and liquid phase. At a high fraction of bubbles, the bubble fraction varies with depth, as denoted in Figure 9, and the drainage in such foam is complicated (Cantat et al., 2010). Coarsening and coalescence of bubbles occur, which vary the

bubble size with time and depth (Maurdev et al., 2006; Sato & Sumita, 2007). Compaction induced by the bubble deformation is also expected (Bercovici & Ricard, 2003; Huber & Parmigiani, 2018; McKenzie, 1984). These processes are essential to generate the large cavity at the top of the bubbly flow, but the film rupture process of the viscous surfactant-free liquid is not well established (Ohashi et al., 2022), and we here use Equations 17–19 for an order estimate.

Next, we estimate the time scale to develop the liquid-rich bottom layer. In the experiment Figure 4b, $\phi_b = 0.69$, which is higher than ϕ_{bmax} , but considering the vertical variation of the bubble fraction, it is appropriate to use Equation 18 for a minimum estimate. Using the parameters for the experiment in Figure 4b, assuming a bubble radius of 1 mm and a bubble fraction at the base of the bubble-rich layer $\phi_b \sim 0.64$, which is appropriate for a wet foam (Cantat et al., 2010), we obtain $v_h \sim 0.07 \text{ mm s}^{-1}$. Dividing the bubble size by the hindered rise velocity, we estimate that a liquid layer with a thickness of the bubble size develops in $\sim 10 \text{ s}$. Figure 5a indicates that the power index of the bubbly flow becomes close to $\frac{1}{3}$, a value close to Newtonian fluid, after $\sim 10 \text{ s}$ elapsed. This may be because deformation is concentrated in the bottom Newtonian fluid layer.

The liquid-rich layer can explain the limited effect of bubbles on slowing the flow velocity. The bubble fraction of $\phi_b = 0.69$ for the experiment in Figure 4b can increase the viscosity 100 times relative to pure liquid (Figure 2). The density has also decreased to about 30% of the pure liquid. Together, these should lead to slowing down the flow $< 1/100$. However, the velocity reduction is $\sim 1/10$ (Figure 4b). The non-Newtonian characteristic might be a source of this discrepancy, but the power index of $\frac{1}{3}$ suggests that the liquid-rich layer behaves as a Newtonian fluid (Figure 5a). One possible interpretation is that the bottom liquid-rich layer helps to lubricate the bubbly flow, and the increase of effective viscosity is less than the above estimate. In our particle-bearing bubbly fluid, the particle density is close to that of the liquid phase, and therefore the particles do not segregate as fast as the bubbles. We also note that the volume fraction of particles is less than the close packing (i.e., $0.35 < \phi_{max} = 0.64$), which is too small to generate large yield stress. Thus, the vertical separation of bubbles could cause the flow to resume (Figure 4c). If the particles are denser than the liquid phase or its volume fraction is close to $\phi_{max} = 0.64$, the bottom of the bubble-poor layer concentrates with particles, which increases the effective viscosity.

The above discussion provides estimates of the orders of magnitude rather than a quantitative analysis. This is because our bubbly fluid has size distributions that affect the effective viscosity, and the quantitative estimate and control of bubble properties are quite difficult.

6. Implication for a Real Lava Flow

6.1. Estimated Range of the Capillary Number in the Lava Flow

Figure 8 demonstrates that we can estimate Ca for individual bubbles in a flow going down a slope only from the fluid thickness and bubble size. This is because the viscosity cancels out, and other parameters are relatively constant. In our experiments, $Ca < 1$, and bubble deformation is not significant (Figure 8). In this section, we use Figure 8 to explore the range of Ca expected for natural lava flows.

The possible range for real lava flows (orange region) straddles both areas of $Ca < 1$ and $Ca > 1$. In particular, low viscosity basaltic flows close to the source region, in confined channels, over steep slopes, or that are several meters thick, can experience rapid velocities and high shear rates and high Ca. Indeed, field viscosity measurements of paho'e'ho'e magma using rotational viscometer indicate that deforming bubble decreases the effective viscosity from 700 to 380 Pa s, where the sample has vesicularity of 0.5, bubble size of 0.34 mm, and the crystallinity of few vol.% (Chevrel et al., 2018). This measurement was conducted under high shear rate of $> 1 \text{ s}^{-1}$, which may be a rare condition within a natural lava flow. We here note that the larger bubbles deform more easily (Equation 4), and larger bubbles are abundant in a real lava flow. In such conditions, even a flow with a small shear rate may cause viscosity decrease as a consequence of bubble deformation.

We here provide a possible example in the field for viscosity decreases and increases associated with changes in Ca. Figures 10a and 10b show an overflow from the main lava flow from Ahu'a'ilā'au (Fissure 8) vent. The overflow leaves the main lava flow from the edge of the levee at 1.9 km downstream from the vent, and forms fingers after $\sim 100 \text{ m}$ of flow. The velocity of the overflow in this narrow channel is $> 0.5 \text{ m s}^{-1}$ but in the fingers, it is $\leq 0.05 \text{ m s}^{-1}$. Here, the lava flow velocity depends on the flow thickness, slope angle, and viscosity

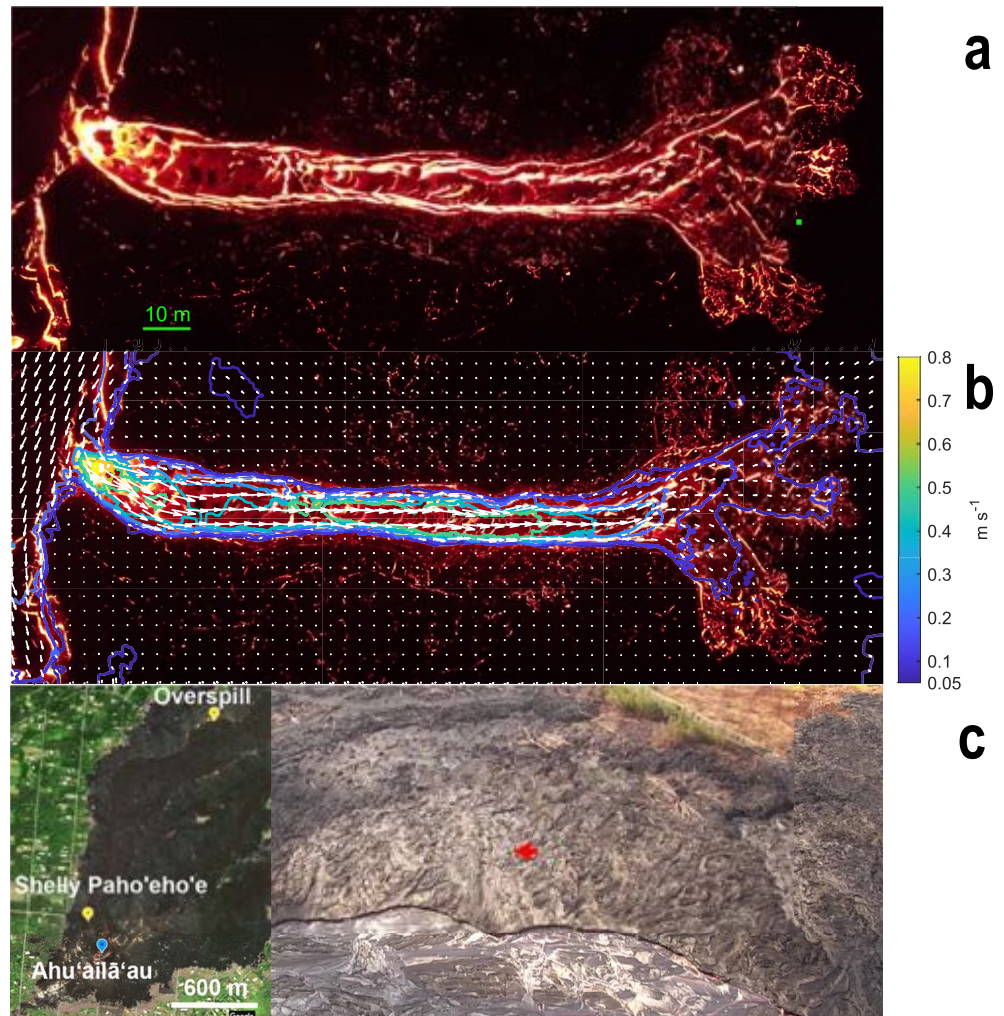


Figure 10. (a) Picture (upper panel) and (b) velocity (lower panel) of channelized overflow located ~ 1.9 km downstream from Ahu'aillā'au (Fissure 8) vent on 26 June at 3:31 a.m. HST (19.47679°N , $154.90153^{\circ}\text{W}$), with an estimated drone flight height of 142 m. The estimated scale is denoted as the green scale bar. The velocity field is obtained by 3 s time difference. The original video is recorded from a moving drone. We adjusted the field of view based on the location at the green square but could not remove all migration. The calculated slow velocity outside the overflow may be originated from the movement of the camera. (c) The daytime view of the region shown in Figures 10a and 10b on 27 June. The gray ribbon run off the main lava flow pointed by the red arrow is the solidified overflow shown in Figures 10a and 10b. The view angle is rotated 90° from Figures 10a and 10b. The inset shows the locations of overflow in Figure 10 and shelly paho'eho'e in Figure 1. The original movies are from DeSmither et al. (2021), and the inset picture was downloaded from Google earth in 2021 October.

(Equation 14). The daytime view of the solidified overflow (Figure 10c), suggests that the flow thickness and slope do not change with location significantly. Cooling and increasing crystallinity are major controlling factors of lava viscosity in general (Harris et al., 2009; Lipman & Banks, 1987), yet here the overflow emplacement time (~ 200 s) is too short to allow cooling to play a significant role in slowing the flow.

One possible interpretation is that the change in Ca, and the associated increase in viscosity, are responsible for the slowing of the overflow flow. The melt viscosity is estimated as 64 Pa s from the viscosity measurements (Soldati et al., 2021). Bubbles and crystals increase the effective viscosity to 4.9 times the liquid viscosity (Gansecki et al., 2019), resulting in the three-phase bulk viscosity becoming 290 Pa s . With bubble radius of 20 mm, $\Gamma = 0.4 \text{ N m}^{-1}$, shear rate of 0.1 s^{-1} as a ratio of flow velocity 0.5 m s^{-1} to the half of channel width 5 m, the estimated $\text{Ca} \sim 1$. If the depth of the channel is shallower than 5 m, which is plausible, the shear rate associated with the vertical velocity profile is higher than 0.1 s^{-1} , so smaller bubbles can deform. Large bubbles ($R > 0.02 \text{ m}$) exceed $\text{Ca} > 1$ and can deform, which decreases the effective viscosity and accelerates the

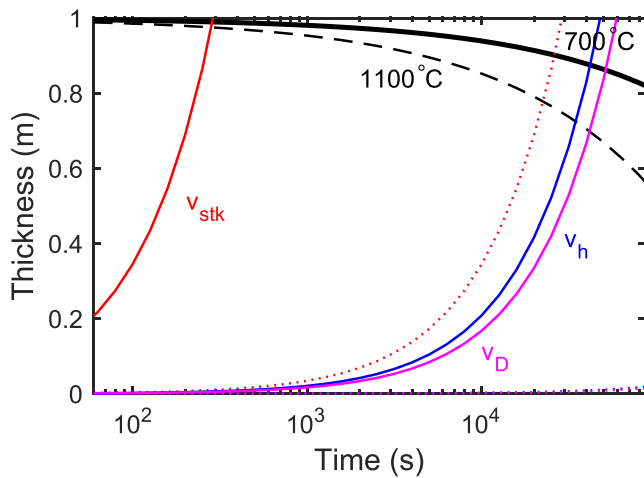


Figure 11. Time evolution of cold crust and liquid-rich bottom layer thicknesses for a 1-m thick lava flow over 1 day. The black curves show the thicknesses of the cooled layer estimated from Equation 20 using $\kappa = 2.6 \times 10^{-7} \text{ m}^2 \text{ s}^{-1}$, $T_a = 25 \text{ }^\circ\text{C}$, and $T_e = 1,168 \text{ }^\circ\text{C}$. The glass transition temperature is $\sim 700 \text{ }^\circ\text{C}$ (Ryan & Sammis, 1981). The liquid viscosity at T_e is 64 Pa s and increases to 218 Pa s at $1,100 \text{ }^\circ\text{C}$ (Soldati et al., 2021). Red, blue, and pink curves are the estimated thicknesses of the liquid-rich layer from Equations 17–19 assuming $\phi_b = 0.64$ and $\rho_l = 2,700 \text{ kg m}^{-3}$. Solid and dotted curves are for $R = 5 \text{ mm}$, and 0.5 mm , respectively.

flow. Such a rapid flow increases Ca, deforms bubbles, and enhances coalescence (Okumura et al., 2006), which may facilitate the formation of giant bubbles. The larger bubbles are more buoyant and concentrate at the top of the flow front. In contrast, smaller bubbles $R < 0.02 \text{ m}$ are below $\text{Ca} < 1$ and increase the effective viscosity. Here, smaller bubbles may be left in the lava because of slow ascending velocity. Consequently, the effective viscosity of the lava flow increases at the flow front. If the shear rate becomes too high, the flow may disrupt the giant bubbles and generate smaller ones (Stein & Spera, 1992), contributing to reducing Ca suddenly.

Different from our experiments, fresh less viscous lava is supplied from the upstream, which could generate a local viscosity contrast in a lava flow to cause viscous fingering (Bischofberger et al., 2014; Chen et al., 2017; Homsy, 1987; Nittmann et al., 1985; Oppenheimer et al., 2015). The outer shell of each finger may be eventually solidified and the ascending giant bubbles accumulate beneath it. When the bubbles are concentrated, the chance for bubbles to come into contact with each other increases. Assuming that the bubble coalescence is governed by percolation, the increase of local bubble fraction is expected to enhance the coalescence of bubbles to make larger bubbles (Gaonac'h et al., 2003; Giachetti et al., 2019; Rust & Cashman, 2011). Larger bubbles generated by coalescence accelerate gravitational drainage in the bubble film (Nguyen et al., 2013). Drainage makes the bubble film thinner than critical for rupture. Thus, the closely located bubbles eventually coalesce to make a huge cavity at the end of the flow beneath the solidified crust.

6.2. Solidification of the Lava Surface

As shown in Figure 1, a large cavity with a length scale of $>1 \text{ m}$ exists without an outlet, suggesting that initially the flow contained voluminous bubbles and then bubbles concentrated at the flow front. The measured vesicularity of the lava flow erupted during the 2018 LERZ eruption Kīlauea Volcano, Hawai'i is $0.5 \leq \phi_b \leq 0.82$ (Patrick et al., 2019). If bubble separation occurs in a patch of lava with a volume of 1 m^3 and an initial vesicularity of 0.82 becomes finally 0.5, a cavity with a volume of 0.64 m^3 emerges. Thus, the vertical bubble separation likely generated a shelly paho'ehoe.

The lava flow cools from the surface, so bubble separation needs to occur before the solidification. Lava flows erupt at high temperatures, such as the basaltic lava at Hawaii ($>1,000 \text{ }^\circ\text{C}$). The large temperature difference with the ambient environment cools the lava flow. Heat loss from the lava surface is caused by radiation and convection of surrounding air (Griffiths, 2000).

In Figure 11, we estimate the time scale to develop a solidified crust by the thermal diffusion, where a hot lava is contacting an atmosphere with a constant temperature

$$L_c = 2\sqrt{\kappa t} \operatorname{erfc}^{-1} \left(\frac{T - T_a}{T_e - T_a} \right) \quad (20)$$

where L_c is the thickness of the cooled lava crust to a given temperature, t is time, T is the glass transition or a certain temperature, T_a is atmospheric temperature, T_e is eruptive temperature. We here estimate the thermal diffusivity by the method used in Namiki et al. (2021), $\kappa = (k_m(1 - \phi_b) + k_a\phi_b)/[\rho_l(1 - \phi_b)C_p]$, where $k_m = 1.22 \text{ W m}^{-1} \text{ K}^{-1}$ and $k_a = 0.166 \text{ W m}^{-1} \text{ K}^{-1}$ are thermal conductivity of bubble-free magma and steam, respectively, and $C_p = 2,300 \text{ J K}^{-1} \text{ kg}^{-1}$ is heat capacity of melt. We here neglect the effect of bubbles on heat capacity because its effect based on the mass fraction is quite small. The measured vesicularity for the LERZ eruption is 0.5–0.82 (Patrick et al., 2019). For this vesicularity range, the range of thermal diffusivity is narrow $2.2 \times 10^{-7} < \kappa < 3.2 \times 10^{-7} \text{ m}^2 \text{ s}^{-1}$, so we used an average value of $2.6 \times 10^{-7} \text{ m}^2 \text{ s}^{-1}$.

The surface temperature of the lava flow is higher than the atmospheric temperature (Fink & Griffiths, 1990). The hot lava heats the air above it and drives air convection, which cools the lava, and then the surface temperature adjusts to the atmosphere (Moitra et al., 2018; Stroberg et al., 2010). Our estimate assumes the constant atmospheric temperature of the lava surface in Equation 20, which implies neglecting the time for surface cooling, and results in a maximum estimate of the solidified crust growth. Convection may occur inside the lava flow, enhancing the heat transport from the inside lava flow to the atmosphere. However, a viscous boundary layer develops at the surface of the lava, in which heat transportation is governed by thermal conduction (Griffiths et al., 2003).

The black solid curve in Figure 11 shows the glass transition temperature of 700 °C (Ryan & Sammis, 1981) and suggests that lava flow with a typical thickness ($\gg 10^{-1}$ m) takes >7 hr to solidify. Eruptive temperature is assumed as $T_e = 1,168$ °C, and liquid viscosity is 64 Pa s (Soldati et al., 2021). The dashed black curve (1,100 °C) indicates the onset of viscosity increase to 218 Pa s (Soldati et al., 2021). The growing liquid-rich layer thickness is calculated by multiplying the time and estimated velocities from Equations 17–19. If the bubble size is relatively large (>0.01 m), bubble separation easily occurs, but this is not the case when the bubble size is small <1 mm. It is reasonable to consider that the internal bubbles have already experienced the coalescence and have a large size at the end of a lava flow.

It is helpful to consider a dimensionless number indicating whether bubble separation or solidification by cooling is more dominant. The thickness ratio of the liquid-rich layer L_l and the cooled upper crust L_c makes a dimensionless number. The evaluation of liquid-rich layer growth depends on the specific situation (Equations 17–19), but all cases depend on v_{stk} , as defined by Equation 17. We here use v_{stk} and neglect some constants for simplicity, and thus obtain

$$\frac{L_l}{L_c} = \frac{R^2 \rho_l g t / \eta}{\sqrt{\kappa t}} \quad (21)$$

We note $L_l/L_c \propto \sqrt{t}$, and bubble radius R will increase with time. Thus, Equation 21 indicates that, if the flow thickness is sufficiently thick not to solidify too fast, the effect of bubble separation becomes more dominant with time. In a real lava flow, bubbles accumulate beneath the solidified upper crust which prevent growth of cold crust. We thus conclude that bubble separation can occur to form a cavity in a shelly paho'ehoe.

In Figures 4c and 5a, we observed the resuming of the stopped flow by the vertical separation of bubbles. This phenomenon is caused by the balance between the gravitational driving force of flow $\rho_l(1 - \phi_b)gh \sin \theta$ and the yield strength τ_y . For highly crystalline magma, the yield strength will be high so that flow is likely to stop (Castruccio et al., 2014). In this case, the effective viscosity of the magma is also high, and bubble separation takes a long time. High bubble fraction also causes yield strength, but its value can be lower than that induced only by crystallinity (Birnbaum et al., 2021; Hohler & Cohen-Addad, 2005). Field measurements of yield strength of basaltic lava flow are in the order of 10^2 – 10^3 Pa (Chevrel et al., 2019). Assuming a yield strength of $\tau_y \sim 10^3$ Pa, melt density of $\rho = 2,700$ kg m $^{-3}$, vesicularity of 0.7, and slope angle of 25°, a 0.3 m thick flow would stop. Figure 11 suggests bubble separation can occur before the solidification in lava flows with a thickness of 0.3 m. We conclude that stopping and resuming of flow by changing the microstructure-dependent yield stress can occur in a natural lava flow.

7. Conclusion

We conducted a series of experiments of analog lava flows using bubbly corn syrup suspensions at a regime dominated by bubble surface tension (the capillary number, $Ca < 1$), where bubbles are expected to increase the effective viscosity of the suspension compared to the liquid viscosity. This regime is relevant for slow moving natural lava flows such as the flow end of thin overspills from main channels, and can work to slow the flow further than cooling alone. We identified a possibly non-Newtonian behavior during the early stages of the flow of bubbly suspensions, but then a return to Newtonian behavior. Liquid segregation and flow localization occurred in sections where bubble-poor, and thus a denser and also less viscous (since $Ca < 1$) fluid advanced faster than the rest of the flow. In natural lava flows, $Ca > 1$ can occur, which can accelerate flow velocity and enhance bubble coalescence. Large bubbles and liquid-rich regions can accumulate at the flow front. A bubble-rich region generated by the vertical separation might be an origin of shelly paho'ehoe.

Data Availability Statement

The video used for the overspill analysis (Figure 10) is currently available through the USGS ScienceBase (DeSmither et al., 2021). For the calculation on velocity field in Figures 6 and 10, we used optical flow (Sun et al., 2010).

Acknowledgments

We thank Matthew R. Patrick and USGS field crews for their help in the field and Ikuro Sumita for providing the laser displacement sensor. AN is supported by JSPS KAKENHI 17KK0092 and 19H00721, and Nagoya University Research Fund. EL, JBi, and JBa were supported by NSF Grants EAR-1654588 and EAR-1929008. JBa was supported by NSF graduate research fellowship.

References

- Bagdassarov, N., & Dingwell, D. (1992). A rheological investigation of vesicular rhyolite. *Journal of Volcanology and Geothermal Research*, *50*, 307–322. [https://doi.org/10.1016/0377-0273\(92\)90099-Y](https://doi.org/10.1016/0377-0273(92)90099-Y)
- Balmforth, N. J., Craster, R. V., Rust, A. C., & Sassi, R. (2007). Viscoplastic flow over an inclined surface. *Journal of Non-Newtonian Fluid Mechanics*, *142*, 219–243. <https://doi.org/10.1016/j.jnnfm.2006.07.013>
- Bercovici, D., & Ricard, Y. (2003). Energetics of a two-phase model of lithospheric damage, shear localization and plate-boundary formation. *Geophysical Journal International*, *152*, 581–596. <https://doi.org/10.1046/j.1365-246X.2003.01854.x>
- Biass, S., Orr, T. R., Houghton, B. F., Patrick, M. R., James, M. R., & Turner, N. (2019). Insights into pahoehoe lava emplacement using visible and thermal structure-from-motion photogrammetry. *Journal of Geophysical Research: Solid Earth*, *124*, 5678–5695. <https://doi.org/10.1029/2019JB017444>
- Birnbaum, J., Lev, E., & Llewellyn, E. W. (2021). Rheology of three-phase suspensions determined via dam-break experiments. *Proceedings of the Royal Society A*, *477*, 20210394. <https://doi.org/10.1098/rspa.2021.0394>
- Bischofberger, I., Ramachandran, R., & Nagel, S. R. (2014). Fingering versus stability in the limit of zero interfacial tension. *Nature Communications*, *5*, 5265. <https://doi.org/10.1038/ncomms6265>
- Cantat, I., Cohen-Addad, S., Elias, F., Graner, F., Hohlner, R., Pitois, O., et al. (2010). *Les mousses: Structure et dynamique*. Yoshioka Shoten.
- Cashman, K. V., Mangan, M. T., & Newman, S. (1994). Surface degassing and modifications to vesicle size distributions in active basalt flows. *Journal of Volcanology and Geothermal Research*, *61*, 45–68. [https://doi.org/10.1016/0377-0273\(94\)00015-8](https://doi.org/10.1016/0377-0273(94)00015-8)
- Castruccio, A., Rust, A., & Sparks, R. (2010). Rheology and flow of crystal-bearing lavas: Insights from analogue gravity currents. *Earth and Planetary Science Letters*, *297*(3), 471–480. <https://doi.org/10.1016/j.epsl.2010.06.051>
- Castruccio, A., Rust, A., & Sparks, R. (2014). Assessing lava flow evolution from post-eruption field data using Herschel-Bulkley rheology. *Journal of Volcanology and Geothermal Research*, *275*, 71–84. <https://doi.org/10.1016/j.jvolgeores.2014.02.004>
- Chen, Y.-F., Fang, S., Wu, D.-S., & Hu, R. (2017). Visualizing and quantifying the crossover from capillary fingering to viscous fingering in a rough fracture. *Water Resources Research*, *53*, 7756–7772. <https://doi.org/10.1002/2017WR021051>
- Chevrel, M. O., Favalli, M., Villeneuve, N., Harris, A. J. L., Fornaciari, A., Richter, N., et al. (2021). Lava flow hazard map of Piton de la Fournaise volcano. *Natural Hazards and Earth System Sciences*, *21*(8), 2355–2377. <https://doi.org/10.5194/nhess-21-2355-2021>
- Chevrel, M. O., Harris, A. J. L., James, M. R., Calabrò, L., Gurioli, L., & Pinkerton, H. (2018). The viscosity of pāhoehoe lava: In situ syn-eruptive measurements from Kīlauea, Hawaii. *Earth and Planetary Science Letters*, *493*, 161–171. <https://doi.org/10.1016/j.epsl.2018.04.028>
- Chevrel, M. O., Pinkerton, H., & Harris, A. J. (2019). Measuring the viscosity of lava in the field: A review. *Earth-Science Reviews*, *196*, 102852. <https://doi.org/10.1016/j.earscirev.2019.04.024>
- Coussot, P., Nguyen, Q., Huynh, H. T., & Bonn, D. (2002). Avalanche behavior in yield stress fluids. *Physical Review Letters*, *88*, 175501. <https://doi.org/10.1103/PhysRevLett.88.175501>
- Craster, R. V., & Matar, O. K. (2009). Dynamics and stability of thin liquid films. *Reviews of Modern Physics*, *81*, 1131–1198. <https://doi.org/10.1103/RevModPhys.81.1131>
- Davis, R. H., & Birdsell, K. H. (1988). Hindered settling of semidilute monodisperse and polydisperse suspensions. *AIChE Journal*, *34*, 123–129. <https://doi.org/10.1002/aic.690340114>
- deGraffenried, R., Hammer, J., Dietterich, H., Perroy, R., Patrick, M., & Shea, T. (2021). Evaluating lava flow propagation models with a case study from the 2018 eruption of Kīlauea Volcano, Hawai‘i. *Bulletin of Volcanology*, *83*, 65. <https://doi.org/10.1007/s00445-021-01492-x>
- DeSmither, L. G., Diefenbach, A. K., & Dietterich, H. R. (2021). *Unoccupied aircraft systems (UAS) video of the 2018 lower East Rift Zone eruption of Kīlauea volcano, Hawaii*. U.S. Geological Survey data release. <https://doi.org/10.5066/P9BVENTG>
- Didden, N., & Maxworthy, T. (1982). The viscous spreading of plane and axisymmetric gravity currents. *Journal of Fluid Mechanics*, *121*, 27–42. <https://doi.org/10.1017/S0022112082001785>
- Dietterich, H. R., Cashman, K. V., Rust, A. C., & Lev, E. (2015). Diverting lava flows in the lab. *Nature Geoscience*, *8*, 494–496. <https://doi.org/10.1038/ngeo2470>
- Dietterich, H. R., Diefenbach, A. K., Soule, S. A., Zoeller, M. H., Patrick, M. P., Major, J. J., & Lundgren, P. R. (2021). Lava effusion rate evolution and erupted volume during the 2018 Kīlauea lower East Rift Zone eruption. *Bulletin of Volcanology*, *83*, 25. <https://doi.org/10.1007/s00445-021-01443-6>
- Di Fiore, F., Vona, A., Kolzenburg, S., Mollo, S., & Romano, C. (2021). An extended rheological map of pāhoehoe—‘a‘ā Transition. *Journal of Geophysical Research: Solid Earth*, *126*, e2021JB022035. <https://doi.org/10.1029/2021JB022035>
- Favalli, M., Fornaciari, A., Mazzarini, F., Harris, A., Neri, M., Behncke, B., et al. (2010). Evolution of an active lava flow field using a multitemporal LIDAR acquisition. *Journal of Geophysical Research*, *115*, B11203. <https://doi.org/10.1029/2010JB007463>
- Fink, J. H., & Griffiths, R. W. (1990). Radial spreading of viscous-gravity currents with solidifying crust. *Journal of Fluid Mechanics*, *221*, 485–509. <https://doi.org/10.1017/S0022112090003640>
- Fujita, E., Hidaka, M., Goto, A., & Umino, S. (2009). Simulations of measures to control lava flows. *Bulletin of Volcanology*, *71*, 401–408. <https://doi.org/10.1007/s00445-008-0229-7>
- Gansecki, C., Lee, R. L., Shea, T., Lundblad, S. P., Hon, K., & Parcheta, C. (2019). The tangled tale of Kīlauea’s 2018 eruption as told by geochemical monitoring. *Science*, *366*, eaaz0147. <https://doi.org/10.1126/science.aaz0147>
- Gaonac’h, H., Lovejoy, S., & Schertzer, D. (2003). Percolating magmas and explosive volcanism. *Geophysical Research Letters*, *30*(11), 1559. <https://doi.org/10.1029/2002GL016022>
- Gaonac’h, H., Stix, J., & Lovejoy, S. (1996). Scaling effects on vesicle shape, size and heterogeneity of lavas from Mount Etna. *Journal of Volcanology and Geothermal Research*, *74*, 131–153. [https://doi.org/10.1016/S0377-0273\(96\)00045-5](https://doi.org/10.1016/S0377-0273(96)00045-5)
- Gasparini, A. (2020). Corn syrup reveals how bubbles affect lava’s flow. *Eos, Transactions American Geophysical Union*, *101*. <https://doi.org/10.1029/2020EO152868>

- Giachetti, T., Gonnermann, H. M., Gardner, J. E., Burgisser, A., Hajimirza, S., Earley, T. C., et al. (2019). Bubble coalescence and percolation threshold in expanding rhyolitic magma. *Geochemistry, Geophysics, Geosystems*, 20, 1054–1074. <https://doi.org/10.1029/2018GC008006>
- Gregg, T. K., & Fink, J. H. (2000). A laboratory investigation into the effects of slope on lava flow morphology. *Journal of Volcanology and Geothermal Research*, 96(3), 145–159. [https://doi.org/10.1016/S0377-0273\(99\)00148-1](https://doi.org/10.1016/S0377-0273(99)00148-1)
- Griffiths, R. W. (2000). The dynamics of lava flows. *Annual Review of Fluid Mechanics*, 32, 477–518. <https://doi.org/10.1146/annurev.fluid.32.1.477>
- Griffiths, R. W., Kerr, R. C., & Cashman, K. V. (2003). Patterns of solidification in channel flows with surface cooling. *Journal of Fluid Mechanics*, 496, 33–62. <https://doi.org/10.1017/S0022112003006517>
- Gurioli, L., Colo', L., Bollasina, A. J., Harris, A. J. L., Whittington, A., & Ripepe, M. (2014). Dynamics of Strombolian explosions: Inferences from field and laboratory studies of erupted bombs from Stromboli volcano. *Journal of Geophysical Research: Solid Earth*, 119, 319–345. <https://doi.org/10.1002/2013JB010355>
- Halverson, B. A., Whittington, A. G., Kenderes, S. M., Hammer, J. E., Dieterich, H. R., Lev, E., et al. (2021). *Correlation of calculated cooling rates with textural variations of the Fissure 8 flow field, Kīlauea 2018: A method for determination of primary and secondary textures*. AGU fall meeting abstract.
- Harris, A. J. L., Favalli, M., Mazzarini, F., & Hamilton, C. W. (2009). Construction dynamics of a lava channel. *Bulletin of Volcanology*, 71, 459. <https://doi.org/10.1007/s00445-008-0238-6>
- Harris, A. J. L., & Rowland, S. (2001). FLOWGO: A kinematic thermo-rheological model for lava flowing in a channel. *Bulletin of Volcanology*, 63, 20. <https://doi.org/10.1007/s004450000120>
- Harris, A. J. L., & Rowland, S. K. (2015). Chapter 17—Lava flows and rheology. In H. Sigurdsson (Ed.), *The encyclopaedia of volcanoes* (2nd ed., pp. 321–342). Amsterdam: Academic Press. <https://doi.org/10.1016/B978-0-12-385938-9.00017-1>
- Herd, R. A., & Pinkerton, H. (1997). Bubble coalescence in basaltic lava: Its impact on the evolution of bubble populations. *Journal of Volcanology and Geothermal Research*, 75, 137–157. [https://doi.org/10.1016/S0377-0273\(96\)00039-X](https://doi.org/10.1016/S0377-0273(96)00039-X)
- Herschel, W. H., & Bulkley, R. (1926). Konsistenzmessungen von Gummi-Benzollösungen. *Kolloid Zeitschrift*, 39, 291. <https://doi.org/10.1007/bf01432034>
- Hohler, R., & Cohen-Addad, S. (2005). Rheology of liquid foam. *Journal of Physics: Condensed Matter*, 17, R1041–R1069. <https://doi.org/10.1088/0953-8984/17/41/r01>
- Homsy, G. M. (1987). Viscous fingering in porous media. *Annual Review of Fluid Mechanics*, 19, 271–311. <https://doi.org/10.1146/annurev.fl.19.010187.001415>
- Huber, C., & Parmigiani, A. (2018). A physical model for three-phase compaction in silicic magma reservoirs. *Journal of Geophysical Research: Solid Earth*, 123, 2685–2705. <https://doi.org/10.1002/2017JB015224>
- Huppert, H. E. (1982a). Flow and instability of a viscous current down a slope. *Nature*, 300, 427–429. <https://doi.org/10.1038/300427a0>
- Huppert, H. E. (1982b). The propagation of two-dimensional and axisymmetric viscous gravity currents over a rigid horizontal surface. *Journal of Fluid Mechanics*, 121, 43–58. <https://doi.org/10.1017/S0022112082001797>
- Jenkins, S., Day, S., Faria, B., & Fonseca, J. (2017). Damage from lava flows: Insights from the 2014–2015 eruption of Fogo, Cape Verde. *Journal of Applied Volcanology*, 6(1), 1–17. <https://doi.org/10.1186/s13617-017-0057-6>
- Jones, A. E. (1943). Classification of lava-surfaces. *Eos, Transactions American Geophysical Union*, 24(1), 265–268. <https://doi.org/10.1029/TR024i001p00265>
- Katz, M. G., & Cashman, K. V. (2003). Hawaiian lava flows in the third dimension: Identification and interpretation of pahoehoe and 'a'a distribution in the KP-1 and SOH-4 cores. *Geochemistry, Geophysics, Geosystems*, 4, 8705. <https://doi.org/10.1029/2001GC000209>
- Kerr, R. C., Griffiths, R. W., & Cashman, K. V. (2006). Formation of channelized lava flows on an unconfined slope. *Journal of Geophysical Research*, 111, B10206. <https://doi.org/10.1029/2005JB004225>
- Klein, J., Mueller, S. P., & Castro, J. M. (2017). The influence of crystal size distributions on the rheology of magmas: New insights from analog experiments. *Geochemistry, Geophysics, Geosystems*, 18, 4055–4073. <https://doi.org/10.1002/2017GC007114>
- Kolzenburg, S., Jaenicke, J., Münzer, U., & Dingwell, D. (2018). The effect of inflation on the morphology-derived rheological parameters of lava flows and its implications for interpreting remote sensing data—A case study on the 2014/2015 eruption at Holuhraun, Iceland. *Journal of Volcanology and Geothermal Research*, 357, 200–212. <https://doi.org/10.1016/j.jvolgeores.2018.04.024>
- Leshner, C. E., & Spera, F. J. (2015). Chapter 5—Thermodynamic and transport properties of silicate melts and magma. In H. Sigurdsson (Ed.), *The encyclopedia of volcanoes* (2nd ed., pp. 113–141). Academic Press. <https://doi.org/10.1016/B978-0-12-385938-9.00005-5>
- Lev, E., Spiegelman, M., Wysocki, R. J., & Karson, J. A. (2012). Investigating lava flow rheology using video analysis and numerical flow models. *Journal of Volcanology and Geothermal Research*, 247–248, 62–73. <https://doi.org/10.1016/j.jvolgeores.2012.08.002>
- Lipman, P., & Banks, N. (1987). *A'a flow dynamics, 1984 Mauna Loa Eruption* (Vol. 1350, pp. 1527–1567). USGS professional paper.
- Lister, J. R. (1992). Viscous flows down an inclined plane from point and line sources. *Journal of Fluid Mechanics*, 242, 631–653. <https://doi.org/10.1017/S0022112092002520>
- Llewellyn, E. W., Mader, H. M., & Wilson, S. D. R. (2002). The rheology of a bubbly liquid. *Proceedings of the Royal Society A Mathematical Physical and Engineering Sciences*, 458, 987–1016. <https://doi.org/10.1098/rspa.2001.0924>
- Llewellyn, E. W., & Manga, M. (2005). Bubble suspension rheology and implications for conduit flow. *Journal of Volcanology and Geothermal Research*, 143, 205–217. <https://doi.org/10.1016/j.jvolgeores.2004.09.018>
- Mader, H., Llewellyn, E., & Mueller, S. (2013). The rheology of two-phase magmas: A review and analysis. *Journal of Volcanology and Geothermal Research*, 257, 135–158. <https://doi.org/10.1016/j.jvolgeores.2013.02.014>
- Manga, M., Castro, J., Cashman, K. V., & Loewenberg, M. (1998). Rheology of bubble-bearing magmas. *Journal of Volcanology and Geothermal Research*, 87, 15–28. [https://doi.org/10.1016/S0377-0273\(98\)00091-2](https://doi.org/10.1016/S0377-0273(98)00091-2)
- Manga, M., & Loewenberg, M. (2001). Viscosity of magmas containing highly deformable bubbles. *Journal of Volcanology and Geothermal Research*, 105(1), 19–24. [https://doi.org/10.1016/S0377-0273\(00\)00239-0](https://doi.org/10.1016/S0377-0273(00)00239-0)
- Maurdev, G., Saint-Jalmes, A., & Langevin, D. (2006). Bubble motion measurements during foam drainage and coarsening. *Journal of Colloid and Interface Science*, 300, 735–743. <https://doi.org/10.1016/j.jcis.2006.03.079>
- McKenzie, D. (1984). The generation and compaction of partially molten rock. *Journal of Petrology*, 25, 713–765. <https://doi.org/10.1093/ptrology/25.3.713>
- Mériaux, C. A., May, D. A., & Jaupart, C. (2022). The impact of vent geometry on the growth of lava domes. *Geophysical Journal International*, 229, 1680–1694. <https://doi.org/10.1093/gji/ggac005>
- Moitra, P., & Gonnermann, H. M. (2015). Effects of crystal shape- and size-modality on magma rheology. *Geochemistry, Geophysics, Geosystems*, 16, 1–26. <https://doi.org/10.1002/2014GC005554>
- Moitra, P., Sonder, I., & Valentine, G. A. (2018). Effects of size and temperature-dependent thermal conductivity on the cooling of pyroclasts in air. *Geochemistry, Geophysics, Geosystems*, 19, 3623–3636. <https://doi.org/10.1029/2018GC007510>

- Møller, P. C. F., Rodts, S., Michels, M. A. J., & Bonn, D. (2008). Shear banding and yield stress in soft glassy materials. *Physical Review E*, 77, 041507. <https://doi.org/10.1103/PhysRevE.77.041507>
- Mueller, S., Llewellyn, E. W., & Mader, H. M. (2011). The effect of particle shape on suspension viscosity and implications for magmatic flows. *Geophysical Research Letters*, 38, L13316. <https://doi.org/10.1029/2011GL047167>
- Namiki, A., Patrick, M. R., Manga, M., & Houghton, B. F. (2021). Brittle fragmentation by rapid gas separation in a Hawaiian fountain. *Nature Geoscience*, 14, 242–247. <https://doi.org/10.1038/s41561-021-00709-0>
- Namiki, A., & Tanaka, Y. (2017). Oscillatory rheology measurements of particle- and bubble-bearing fluids: Solid-like behavior of a crystal-rich basaltic magma. *Geophysical Research Letters*, 44, 8804–8813. <https://doi.org/10.1002/2017GL074845>
- Namiki, A., Tanaka, Y., Okumura, S., Sasaki, O., Sano, K., & Takeuchi, S. (2020). Fragility and an extremely low shear modulus of high porosity silicic magma. *Journal of Volcanology and Geothermal Research*, 392, 106760. <https://doi.org/10.1016/j.jvolgeores.2019.106760>
- Neal, C. A., Brantley, S. R., Antolik, L., Babb, J. L., Burgess, M., Calles, K., et al. (2019). The 2018 rift eruption and summit collapse of Kīlauea Volcano. *Science*, 363(6425), 367–374. <https://doi.org/10.1126/science.aav7046>
- Nguyen, C. T., Gonnermann, H. M., Chen, Y., Huber, C., Maiorano, A. A., Gouldstone, A., & Dufek, J. (2013). Film drainage and the lifetime of bubbles. *Geochemistry, Geophysics, Geosystems*, 14, 3616–3631. <https://doi.org/10.1002/ggge.20198>
- Nittmann, J., Daccord, G., & Stanley, H. (1985). Fractal growth viscous fingers: Quantitative characterization of a fluid instability phenomenon. *Nature*, 314, 141–144. <https://doi.org/10.1038/314141a0>
- Ohashi, M., Toramaru, A., & Namiki, A. (2022). Coalescence of two growing bubbles in a hele–shaw cell. *Scientific Reports*, 12, 1270. <https://doi.org/10.1038/s41598-022-05252-5>
- Okumura, S., Nakamura, M., & Tsuchiyama, A. (2006). Shear-induced bubble coalescence in rhyolitic melts with low vesicularity. *Geophysical Research Letters*, 33, L20316. <https://doi.org/10.1029/2006GL027347>
- Oppenheimer, J., Rust, A., Cashman, K., & Sandnes, B. (2015). Gas migration regimes and outgassing in particle-rich suspensions. *Frontiers in Physics*, 3, 60. <https://doi.org/10.3389/fphy.2015.00060>
- Pal, R. (2003). Rheological behavior of bubble-bearing magmas. *Earth and Planetary Science Letters*, 207(1), 165–179. [https://doi.org/10.1016/S0012-821X\(02\)01104-4](https://doi.org/10.1016/S0012-821X(02)01104-4)
- Patrick, M. R., Dietterich, H. R., Lyons, J. J., Diefenbach, A. K., Parcheta, C., Anderson, K. R., et al. (2019). Cyclic lava effusion during the 2018 eruption of Kīlauea volcano. *Science*, 366. <https://doi.org/10.1126/science.aay9070>
- Pistone, M., Cordonnier, B., Ulmer, P., & Caricchi, L. (2016). Rheological flow laws for multiphase magmas: An empirical approach. *Journal of Volcanology and Geothermal Research*, 321, 158–170. <https://doi.org/10.1016/j.jvolgeores.2016.04.029>
- Richardson, P., & Karlstrom, L. (2019). The multi-scale influence of topography on lava flow morphology. *Bulletin of Volcanology*, 81, 21. <https://doi.org/10.1007/s00445-019-1278-9>
- Robert, B., Harris, A., Gurioli, L., Médard, E., Schlke, A., & Whittington, A. (2014). Textural and rheological evolution of basalt flowing down a lava channel. *Bulletin of Volcanology*, 76, 824. <https://doi.org/10.1007/s00445-014-0824-8>
- Rumpf, M. E., Lev, E., & Wysocki, R. (2018). The influence of topographic roughness on lava flow emplacement. *Bulletin of Volcanology*, 80, 63. <https://doi.org/10.1007/s00445-018-1238-9>
- Rust, A. C., & Cashman, K. V. (2011). Permeability controls on expansion and size distributions of pyroclasts. *Journal of Geophysical Research*, 116, B11202. <https://doi.org/10.1029/2011JB008494>
- Rust, A. C., & Manga, M. (2002). Effects of bubble deformation on the viscosity of dilute suspensions. *Journal of Non-Newtonian Fluid Mechanics*, 104, 53–63. [https://doi.org/10.1016/S0377-0257\(02\)00013-7](https://doi.org/10.1016/S0377-0257(02)00013-7)
- Ryan, M. P., & Sammis, C. G. (1981). The glass transition in basalt. *Journal of Geophysical Research*, 86, 9519–9535. <https://doi.org/10.1029/JB086iB10p09519>
- Sato, M., & Sumita, I. (2007). Experiments on gravitational phase separation of binary immiscible fluids. *Journal of Fluid Mechanics*, 591, 289–319. <https://doi.org/10.1017/S0022112007008257>
- Schlke, A., Whittington, A., Robert, B., Harris, A., Gurioli, L., & Médard, E. (2014). Pahoehoe to ‘a’a transition of Hawaiian lavas: An experimental study. *Bulletin of Volcanology*, 76, 876. <https://doi.org/10.1007/s00445-014-0876-9>
- Shea, T., Houghton, B. F., Gurioli, L., Cashman, K. V., Hammer, J. E., & Hobden, B. J. (2010). Textural studies of vesicles in volcanic rocks: An integrated methodology. *Journal of Volcanology and Geothermal Research*, 190, 271–289. <https://doi.org/10.1016/j.jvolgeores.2009.12.003>
- Shibano, Y., Namiki, A., & Sumita, I. (2012). Experiments on upward migration of a liquid-rich layer in a granular medium: Implications for a crystalline magma chamber. *Geochemistry, Geophysics, Geosystems*, 13, Q03007. <https://doi.org/10.1029/2011GC003994>
- Soldati, A., Farrell, J., Sant, C., Wysocki, R., & Karson, J. (2020). The effect of bubbles on the rheology of basaltic lava flows: Insights from large-scale two-phase experiments. *Earth and Planetary Science Letters*, 548, 116504. <https://doi.org/10.1016/j.epsl.2020.116504>
- Soldati, A., Houghton, B., & Dingwell, D. (2021). A lower bound on the rheological evolution of magmatic liquids during the 2018 Kīlauea eruption. *Chemical Geology*, 576, 120272. <https://doi.org/10.1016/j.chemgeo.2021.120272>
- Stasiuk, M. V., Jaupart, C., Stephen, R., & Sparks, J. (1993). Influence of cooling on lava-flow dynamics. *Geology*, 21, 335–338. [https://doi.org/10.1130/0091-7613\(1993\)021<0335:iocolf>2.3.co;2](https://doi.org/10.1130/0091-7613(1993)021<0335:iocolf>2.3.co;2)
- Stein, D. J., & Spera, F. J. (1992). Rheology and microstructure of magmatic emulsions: Theory and experiments. *Journal of Volcanology and Geothermal Research*, 49(1), 157–174. [https://doi.org/10.1016/0377-0273\(92\)90011-2](https://doi.org/10.1016/0377-0273(92)90011-2)
- Stroberg, T. W., Manga, M., & Dufek, J. (2010). Heat transfer coefficients of natural volcanic clasts. *Journal of Volcanology and Geothermal Research*, 194, 214–219. <https://doi.org/10.1016/j.jvolgeores.2010.05.007>
- Sun, D., Roth, S., & Black, M. J. (2010). Secrets of optical flow estimation and their principles. *Paper presented at 2010 IEEE Computer Society Conference on Computer Vision and Pattern Recognition* (pp. 2432–2439). <https://doi.org/10.1109/CVPR.2010.5539939>
- Swanson, D. A. (1973). Pahoehoe flows from the 1969–1971 Mauna Ulu eruption, Kīlauea volcano, Hawaii. *GSA Bulletin*, 84, 615–626. [https://doi.org/10.1130/0016-7606\(1973\)84<615:pfftmu>2.0.co;2](https://doi.org/10.1130/0016-7606(1973)84<615:pfftmu>2.0.co;2)
- Takeda, S., Ohashi, M., Kuwano, O., Kameda, M., & Ichihara, M. (2020). Rheological tests of polyurethane foam undergoing vesiculation-deformation-solidification as a magma analogue. *Journal of Volcanology and Geothermal Research*, 393, 106771. <https://doi.org/10.1016/j.jvolgeores.2020.106771>
- Truby, J. M., Mueller, S. P., Llewellyn, E. W., & Mader, H. M. (2015). The rheology of three-phase suspensions at low bubble capillary number. *Proceedings of the Royal Society A: Mathematical, Physical & Engineering Sciences*, 471, 20140557. <https://doi.org/10.1098/rspa.2014.0557>
- Turcotte, D., & Schubert, G. (2014). *Geodynamics* (3rd ed.). Cambridge University Press.
- Walker, G. P. L. (1989). Spongy pahoehoe in Hawaii: A study of vesicle-distribution patterns in basalt and their significance. *Bulletin of Volcanology*, 51, 199–209. <https://doi.org/10.1007/BF01067956>
- Wentworth, C. K., & Macdonald, G. A. (1953). Structures and forms of basaltic rocks in Hawaii. *US Geological Survey Bulletin*, 994, 98. <https://doi.org/10.3133/b994>